



HAL
open science

Trinuclear Cyanido-Bridged [Cr₂Fe] Complexes: To Be or not to Be a Single-Molecule Magnet, a Matter of Straightness

Céline Pichon, Nicolas Suaud, Valentin Jubault, Carine Duhayon, Nathalie Guihéry, Jean-Pascal Sutter

► **To cite this version:**

Céline Pichon, Nicolas Suaud, Valentin Jubault, Carine Duhayon, Nathalie Guihéry, et al.. Trinuclear Cyanido-Bridged [Cr₂Fe] Complexes: To Be or not to Be a Single-Molecule Magnet, a Matter of Straightness. *Chemistry - A European Journal*, 2021, 27 (62), pp.15484-15495. 10.1002/chem.202102571 . hal-03424346

HAL Id: hal-03424346

<https://hal.science/hal-03424346>

Submitted on 16 Nov 2021

HAL is a multi-disciplinary open access archive for the deposit and dissemination of scientific research documents, whether they are published or not. The documents may come from teaching and research institutions in France or abroad, or from public or private research centers.

L'archive ouverte pluridisciplinaire **HAL**, est destinée au dépôt et à la diffusion de documents scientifiques de niveau recherche, publiés ou non, émanant des établissements d'enseignement et de recherche français ou étrangers, des laboratoires publics ou privés.

Trinuclear cyanido-bridged [Cr₂Fe] complexes: to be or not to be a SMM, a matter of straightness

Céline Pichon,^{*,a} Nicolas Suaud,^{*,b} Valentin Jubault,^a Carine Duhayon,^a Nathalie Guihéry,^{*,b}
Jean-Pascal Sutter^{*,a}

^a Laboratoire de Chimie de Coordination du CNRS (LCC), Université de Toulouse, CNRS, F-31077
Toulouse, France.

e-mail : sutter@lcc-toulouse.fr ; celine.pichon@lcc-toulouse.fr

^b Laboratoire de Chimie et Physique quantiques (LCPQ), Université de Toulouse, CNRS, 118
route de Narbonne, F-31062 Toulouse, France.

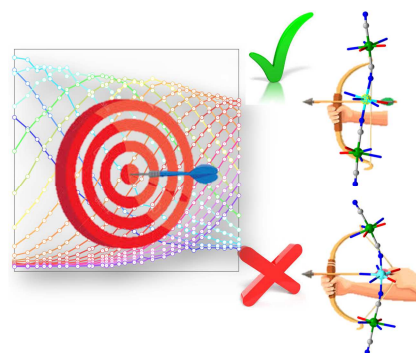
e-mail : suaud@irsamc.ups-tlse.fr nathalie.guihery@irsamc.ups-tlse.fr

Abstract. Trinuclear systems of formula $[\{\text{Cr}(\text{L}^{\text{N}3\text{O}2\text{Ph}})(\text{CN})_2\}_2\text{M}(\text{H}_2\text{L}^{\text{N}3\text{O}2\text{R}})]$ ($\text{M} = \text{Mn}^{\text{II}}$ and Fe^{II} , $\text{L}^{\text{N}3\text{O}2\text{R}2}$ stands for pentadentate ligands) were prepared in order to assess the influence of the bending of the apical $\text{M}-\text{N}\equiv\text{C}$ linkages on the magnetic anisotropy of the Fe^{II} derivatives and in turn on their SMM behaviors. The cyanido-bridged $[\text{Cr}_2\text{M}]$ derivatives were obtained by assembling *trans*-dicyanido Cr^{III} complex $[\text{Cr}(\text{L}^{\text{N}3\text{O}2\text{Ph}2})(\text{CN})_2]^-$ and divalent pentagonal bipyramid complexes $[\text{M}^{\text{II}}(\text{H}_2\text{L}^{\text{N}3\text{O}2\text{R}2})]^{2+}$ with various R substituents ($\text{R} = \text{NH}_2$, cyclohexyl, *S,S*-mandelic) imparting different steric demand to the central moiety of the complexes. A comparative examination of the structural and magnetic properties showed an obvious effect of the deviation from straightness of the $\text{M}-\text{N}\equiv\text{C}$ alignment on the slow relaxation of the magnetization exhibited by the $[\text{Cr}_2\text{Fe}]$ complexes. Theoretical calculations have highlighted important effects of the straightness of the apical $\text{C}-\text{N}-\text{Fe}$ linkages on both the magnetic anisotropy of the Fe^{II} center and the exchange interactions with the Cr^{III} units.

Keywords: Magnetic properties; Single-Molecule Magnet; Pentagonal bipyramid complex; magnetic anisotropy; *Ab initio* calculations

Table of Content Graphic

Cyano-bridged trinuclear $[\text{Cr}^{\text{III}}_2\text{Fe}^{\text{II}}]$ complexes were investigated in order to assess the influence of the bending of the apical $\text{Fe-N}\equiv\text{C}$ linkages on their SMM behaviors. A comparative examination of the structural and magnetic properties showed an obvious effect of the deviation from straightness of the $\text{M-N}\equiv\text{C}$ alignment on the slow relaxation of the magnetization exhibited by the complexes. Theoretical calculations have highlighted important effects on both the magnetic anisotropy of the Fe^{II} center and the exchange interactions with the Cr^{III} units.



INTRODUCTION

Over the past 30 years, the design of molecule-based magnetic materials has become rationalized by means of coordination chemistry tools.^[1-8] The combination of pre-formed complexes, used as building blocks, is an effective approach for the controlled construction of magnetic systems with the desired properties. The choice of the metal ions and bridging ligands provides a remarkable control over the exchange interactions taking place between the magnetic centers^[9-10] while the coordination geometry, ligand field and electronic configuration of transition-metal complexes allows also to tune the local magnetic features like the magnetic anisotropy.^[11-12] However, in many cases the final result remains disappointing and suggests that subtler parameters also play an important role.

Ising-type anisotropic building units are relevant components for rationally preparing Single-Molecule Magnets (SMM) and Single-Chain Magnets (SCM), which are low dimensional molecular compounds with magnetic behavior reminiscent of bulk magnets.^[5, 13-14] In this context, heptacoordinated complexes with robust pentagonal bipyramid coordination geometry (PBP hereafter) are interesting species as they can exhibit substantial magnetic anisotropy with axial Zero-Field Splitting (ZFS) D values ranging between -20 and +40 cm^{-1} .^[15-26] Such complexes can also be used as metalloligands by including in their apical positions groups such as cyanides,^[27] which are certainly the most important bridging ligands in molecular-based magnetic systems, including molecular nanomagnets.^[28-32] Following this approach, SCMs with nearly collinear local anisotropy directions have been obtained from heptacoordinated $[\text{CrL}^{\text{N}3\text{O}2\text{R}}(\text{CN})_2]^-$ ($\text{R} = \text{Ph}, \text{NH}_2$, Scheme 1) and PBP Fe^{II} or Ni^{II} derivatives.^[33-34] These cyanido-bridged systems are characterized by ferromagnetic interactions for CrFe and CrNi systems while they are antiferromagnetic in CrMn species. Interestingly, a trimetallic $[\text{Cr}_2\text{Fe}]$ complex with single anisotropic center, Fe^{II} , was shown to behave as a SMM in zero-field.^[33]

The activation energy for magnetization reversal of nanomagnets is mainly governed by magnetic anisotropy, and exchange interactions stabilizing the ground state in SMMs and controlling the correlation energy in SCMs. Regarding PBP Fe^{II} complexes, it has been shown that their axial magnetic anisotropy, quantified by the D parameter, can be strongly dependent on the type of ligands in the apical positions. Largest $|D|$ value were found when the interactions between the d_{xz} and the d_{yz} orbitals of the metal and the π -orbitals of the apical ligands are identical.^[24] This applies for Cl^- ligands and leads to D values in the order of -15 cm^{-1} for Fe^{II} complexes.^[20] This may also be the case for N-bound cyanido ligands, provided

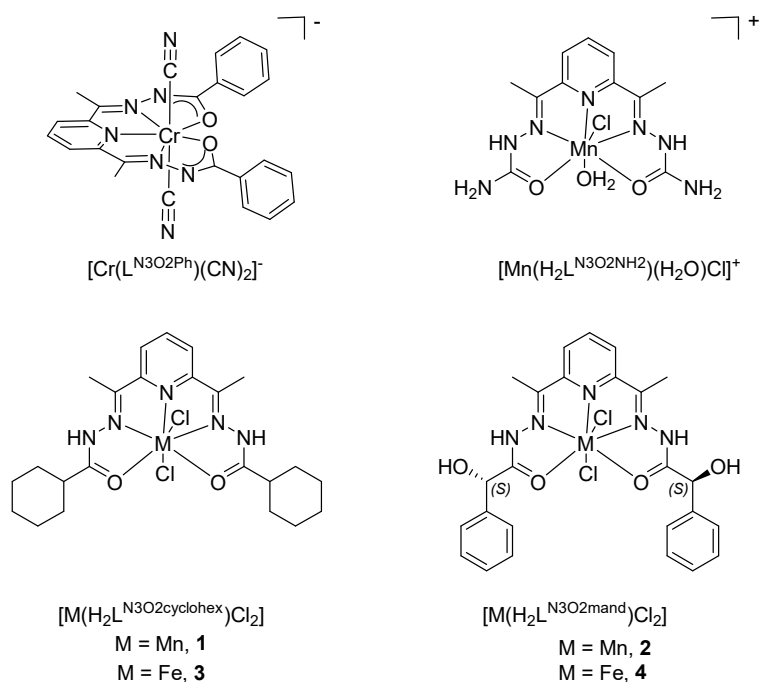
that the CN direction is perpendicular to the pentagonal plane. However, this is hardly true in real compounds where some bending is found. As a result, the π -system of the CN-ligand has a different overlap with the d_{xz} as compared to the d_{yz} orbital of Fe, which changes the energy level of these orbitals that in turn leads to a decrease of $|D|$. The same geometrical parameter may also affect the strengths of the exchange interactions when the CN-bridge mediates magnetic couplings.^[35] In the study described here, we sought to assess the influence of such a deformation on magnetic characteristics of trinuclear $[\text{Cr}_2\text{Fe}]$ SMMs.

By alteration of the peripheral groups on the pentadentate ligands (R in $\text{H}_2\text{L}^{\text{N}3\text{O}2\text{R}}$, Scheme 1) the M-NC-Cr alignment could be modulated in a series of $[\text{Cr}_2\text{M}]$ complexes with $\text{M} = \text{Fe}^{\text{II}}$ and Mn^{II} . A clear effect on the SMM behavior was found for the Fe derivatives, which is rationalized by theoretical calculations revealing substantial alteration of the magnetic anisotropy of the Fe centers and of the Fe-Cr exchange interactions. The magnetically isotropic $[\text{Cr}_2\text{Mn}]$ systems have been used to monitor the changes in the exchange interaction and detect possible intermolecular interactions.

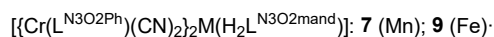
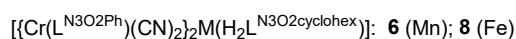
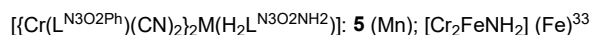
RESULTS AND DISCUSSION

The heptacoordinated complexes of Mn^{II} and Fe^{II} with PBP geometry are based on a pentadentate 2,6-diacetylpyridine bis-(acylhydrazone) ligand, $\text{H}_2\text{L}^{\text{N}3\text{O}2\text{R}}$, with R = NH_2 , cyclohexyl, or *S*-mandelic units (Scheme 1). These substituents have been chosen to vary the steric demand of the central metal complex in the subsequent trinuclear $[\text{Cr}_2\text{M}]$ species formed with $\text{K}[\text{Cr}(\text{L}^{\text{N}3\text{O}2\text{Ph}})(\text{CN})_2]$.

Syntheses. The $\text{H}_2\text{L}^{\text{N}2\text{O}3\text{R}}$ ligands and the heptacoordinated complexes **1** – **4** were prepared by standard procedures detailed in the Experimental section. The trimetallic associations have been carried out using a Cr/M ratio of 2/1. Compound **5**, $[\{\text{Cr}(\text{L}^{\text{N}3\text{O}2\text{Ph}})(\text{CN})_2\}_2\text{Mn}(\text{H}_2\text{L}^{\text{N}3\text{O}2\text{NH}_2})] \cdot 1.5\text{H}_2\text{O} \cdot 4.5\text{MeOH}$, was formed using the conditions settled for the Fe analogue $[\{\text{Cr}(\text{L}^{\text{N}3\text{O}2\text{Ph}})(\text{CN})_2\}_2\text{Fe}(\text{H}_2\text{L}^{\text{N}3\text{O}2\text{NH}_2})]$,^[33] abbreviated $[\text{Cr}_2\text{FeNH}_2]$ hereafter. Cyclohexyl derivatives, $[\{\text{Cr}(\text{L}^{\text{N}3\text{O}2\text{Ph}})(\text{CN})_2\}_2\text{Mn}(\text{H}_2\text{L}^{\text{N}3\text{O}2\text{cyclohex}})] \cdot 5\text{H}_2\text{O} \cdot 2.5\text{MeOH}$, **6**, and $[\{\text{Cr}(\text{L}^{\text{N}3\text{O}2\text{Ph}})(\text{CN})_2\}_2\text{Fe}(\text{H}_2\text{L}^{\text{N}3\text{O}2\text{cyclohex}})] \cdot 7\text{H}_2\text{O} \cdot 2\text{EtOH}$, **8** were obtained in a H_2O -MeOH or EtOH mixture. The chiral complexes $[\{\text{Cr}(\text{L}^{\text{N}3\text{O}2\text{Ph}})(\text{CN})_2\}_2\text{Mn}(\text{H}_2\text{L}^{\text{N}3\text{O}2\text{mand}})] \cdot 13\text{H}_2\text{O}$, **7**, and $[\{\text{Cr}(\text{L}^{\text{N}3\text{O}2\text{Ph}})(\text{CN})_2\}_2\text{Fe}(\text{H}_2\text{L}^{\text{N}3\text{O}2\text{mand}})] \cdot 16\text{H}_2\text{O}$, **9**, were prepared in H_2O .



Trinuclear complexes $[\text{Cr}_2\text{M}]$



Scheme 1: Sketch of the heptacoordinated metal complexes along with their numbering scheme.

Solid state infrared spectra for the $[\text{Cr}_2\text{M}]$ complexes showed two cyanide bands, one showing a noticeable shift from 2130 cm^{-1} in $\text{K}[\text{CrL}^{\text{N}3\text{O}2\text{Ph}}(\text{CN})_2]$. These ν_{CN} bands have been found at 2128 and 2153 cm^{-1} for **5**, 2133 and 2159 cm^{-1} for **6**, 2138 and 2147 cm^{-1} for **7**, 2141 and 2156 cm^{-1} for **8**, and 2135 and 2141 cm^{-1} for **9**, and highlighted the presence of terminal and bridging cyanido ligands.

Crystal structures. All compounds have been obtained in crystalline form and their crystal structures have been solved. General information about the crystallographic investigations can be found in the Experimental section. Compounds **5**, **6**, **7**, **8** and **9** consist in discrete trinuclear complexes of general formula $\{[\text{Cr}(\text{L}^{\text{N}3\text{O}2\text{Ph}})(\text{CN})_2]_2\text{M}(\text{H}_2\text{L}^{\text{N}3\text{O}2\text{R}})\}$ ($\text{M} = \text{Mn}$ or Fe) with different R groups on the ligand coordinated to the central metal. A view of the molecular structure of **5**, **8**, and **9** is given in Figure 1; the other derivatives, as well as a selection of distances and bond angles, can be found in the Supporting Information. In these neutral species, the divalent $[\text{M}(\text{H}_2\text{L}^{\text{N}3\text{O}2\text{R}})]^{2+}$ moieties are located between two $\{[\text{Cr}(\text{L}^{\text{N}3\text{O}2\text{Ph}})(\text{CN})_2]_2\}^-$ units. Only one cyanido of each Cr^{III} is involved in coordination to the

$[M(H_2L^{N3O2R})]$ units whereas each central metal is linked to two Cr by the means of N-bonded cyanido ligands. The cyanido ligands are located in the apical positions of all the PBP coordination spheres, the remaining coordination sites of each metal ion are occupied by a pentadente ligand. The actual deformations of the PBP coordination geometries have been analyzed by Continuous Shape Measures^[36-37] performed with SHAPE^[38] (Table S1). The coordination sphere for all metal ions are close to PBP geometry, with shape distortion values ranging from $S_{PBP} = 0.27$ and 0.78 ($S_{PBP} = 0$ for ideal PBP geometry).

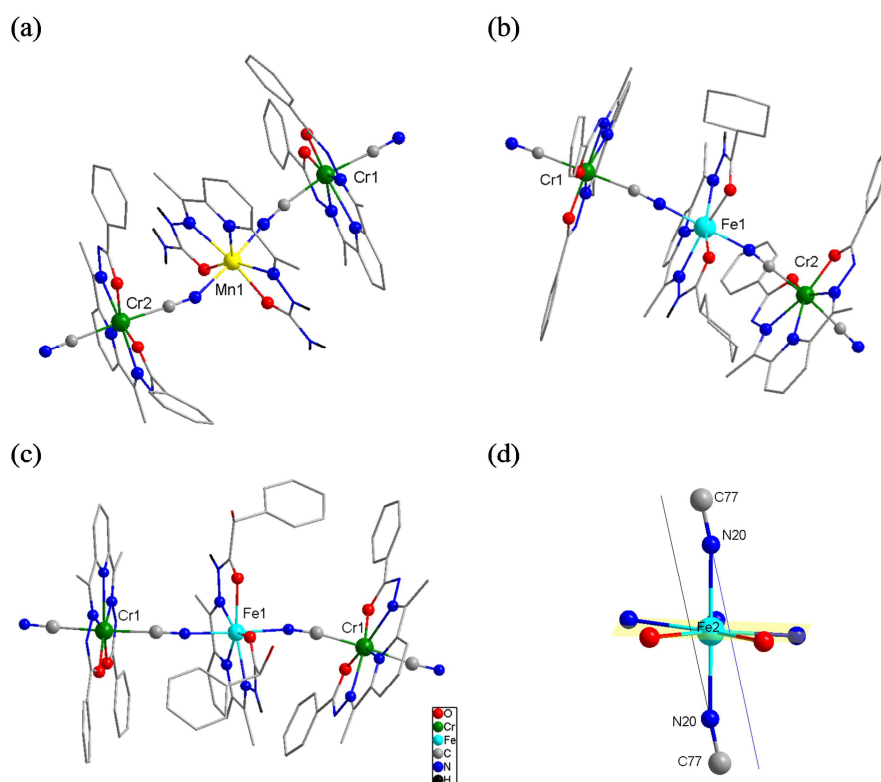


Figure 1. Molecular structure of (a) $[\{Cr(L^{N3O2Ph})(CN)_2\}_2Mn(H_2L^{N3O2NH_2})]$, **5**; (b) $[\{Cr(L^{N3O2Ph})(CN)_2\}_2Fe(H_2L^{N3O2cyclohex})]$, **8** and (c) $[\{Cr(L^{N3O2Ph})(CN)_2\}_2Fe(H_2L^{N3O2mand})]$, **9** (one of the two found in asymmetric unit), (d) N-C bond directions *versus* equatorial plane in **9**.

Regarding the trinuclear organization, besides the R-substituents located at the periphery of the H_2L^{N3O2R} ligand, the $[Cr_2M]$ complexes are mainly differing by the local distortions of the Cr-CN-M linkages and the global molecular bending (Figure S1). The latter can be appreciated by the average $C\equiv N-M$ and $Cr-C\equiv N(M)$ angles that deviate from 180° ($161.05/175.35^\circ$ (**5**), $162.52/175.77^\circ$ (**6**), $166.5/170.24^\circ$ (**7**), $165.26/175.7^\circ$ (**8**), $168.22/168.96^\circ$ (**9**)). In relation with bending of the $C\equiv N-M$ linkage, the divergence of the N-C bond direction from the normal to the pentagonal plane (Figure 1d) varies significantly for

the complexes with angles ranging between 6.08 and 28.8° (Table 1). The latter information is best suited to capture the above-mentioned overlap of the ligand and metal orbitals.

For **5**, the complexes are organized in pairs in the crystal network (Figure S2b-c) with likely H-bonds occurring between the NH₂ and the carbonyl groups of two neighboring manganese entities (N/H...O_{1-x,0.5+y,0.5-z}, 2.86/2.11 Å). The shortest intermolecular metal...metal distance is found between Mn centers with 7.441 Å (Figure S2d). For **6** and **8**, shortest intermolecular distance between paramagnetic centers involves two Cr units with, respectively 8.257 Å and 8.925 Å (Figures S4 and S8). For **7** and **9**, shortest intermolecular metal distance is found between Cr ions with 8.932 and 8.992 Å for **7** and **9**, respectively.

PXRD performed for each bulk sample confirmed that it consisted in a single phase consistent with the crystal structure (Figures S3, S5, S7, S9 and S12).

Mössbauer Spectroscopy. ⁵⁷Fe Mössbauer spectra for **8** and **9** validated the oxidation state 2+ for the Fe center with isomer shifts of 1.18 mm s⁻¹ and 1.22 mm s⁻¹, respectively. The quadrupole splitting, Δ, for the two complexes are somewhat different with values of 3.28 mm s⁻¹ for **8** and 2.89 mm s⁻¹ for **9**; for the related [Cr₂FeNH₂] complex a value of Δ = 2.83 mm s⁻¹ was found.^[33] It has been reported that for PBP Fe^{II} complexes this parameters is very sensitive to the ligands in apical position.^[24]

Table 1. Selected structural and magnetic parameters for **5-9**. The calculated characteristics for $[\text{Cr}_2\text{FeNH}_2]$ were re-assessed using same methodology as for **8** and **9**.

	[Cr ₂ Mn]			[Cr ₂ Fe]		
	5	6	7	[Cr ₂ FeNH ₂] ^a	8	9
Distances (Å)						
M-N(≡C)	2.177/2.189	2.174/2.188	2.213/2.253	2.097/2.114	2.114/2.118	2.170
Angles (°)						
M-N≡C	156.2/165.9	159.5/165.5	164.7/167.7	172.3/160.5	167/163.5	169.8/166.7
CN/⊥ ^b	11.8/28.8	23.5/20.2	11.2/15.5	6.1/26.2	19.0/20.2	9.6/14.0
average	20.3	21.8	13.3	16.1	19.6	11.8
U _{eff} /k _B (K)				22 (0 Oe) ^c	–	19 (0 Oe)/35 (1 kOe) ^c
J _{CrM} (cm ⁻¹)	-4.34	-3.92	-3.30	2.05	2.12	2.80
D _{Fe} (cm ⁻¹)				-25	-11	-20
Calculated (cm ⁻¹)						
D _{Fe} (E _{Fe})				-15.7 (1.76)	-14.4 (2.07)	-23.3(0.97)/ -23.6(0.94) ^d
g _x , g _y , g _z				1.97, 2.04, 2.37	2.00, 2.06, 2.34	1.94, 2.01, 2.48/ 1.94, 2.00, 2.48
D _{Cr} (E _{Cr})				-0.98 (0.29)/-0.86(0.26)	-0.88 (0.24)/-1.05(0.21) ^d	-0.99 (0.20)/-0.97(0.21)
g _x , g _y , g _z				1.95, 1.97, 1.97/ 1.95, 1.97, 1.98	1.95, 1.97, 1.98/ 1.95, 1.97, 1.98 ^d	1.95, 1.97, 1.97/ 1.95, 1.97, 1.97
J _{CrFe} ^e				+2.8/+1.0	+0.1/+1.0 ^d	+2.0/+1.5 ^d

^a from reference [33]; ^b angle between CN axis and normal to the equatorial plane of the M moiety, see Figure 1d; ^c applied DC field; ^d respectively M1 and M2 in Figure 1; ^e DFT with reference Hamiltonian $H = -\mathcal{J}\mathbf{S}_i\mathbf{S}_j$.

Magnetic properties. The temperature dependence of the magnetic susceptibility and the field dependence of the magnetization at 2 K were investigated for all compounds. The [Cr₂Mn] complexes **5** – **7** will be discussed first and then we shall present the results for the [Cr₂Fe] derivatives **8** and **9**.

At 300 K, the $\chi_{\text{M}}T$ values (χ_{M} stands for molar magnetic susceptibility of a Cr₂M unit) of **5**, **6** and **7** are 7.25, 7.30, and 7.55 cm³mol⁻¹K (Figure 2 and Figure S14), in agreement with the Curie constant for two Cr^{III} and one Mn^{II} in the absence of exchange interactions. Upon lowering the temperature, $\chi_{\text{M}}T$ decreases to 0.58, 0.53, and 0.44 cm³ K mol⁻¹ at 2 K, a behavior indicative for antiferromagnetic Cr-Mn interactions. This is supported by the $M = f(H)$ behavior reaching a magnetization below 1.5 μ_{B} for a field of 5 Tesla (Figure S14). Modeling of the $\chi_{\text{M}}T = f(T)$ behaviors has been performed by considering the Cr-Mn exchange interactions, J_{CrMn} ; a possible contribution from intermolecular interactions was considered within a mean-field approximation term, zJ' . This latter parameter may also account for the weak ZFS contribution of the Cr centers revealed by the theoretical calculations (*vide infra*). Analyses were performed using the PHI program,^[39] results are reported according to the Hamiltonian $\hat{H} = -J(\hat{S}_{\text{Cr}1} \cdot \hat{S}_{\text{Mn}} + \hat{S}_{\text{Cr}2} \cdot \hat{S}_{\text{Mn}})$. Best fits to the experimental data gave $J = -4.34 \pm 0.04$ cm⁻¹, $zJ' = -0.20 \pm 0.01$ cm⁻¹ and $g = 1.95 \pm 0.01$ for **5**; $J = -3.92 \pm 0.04$ cm⁻¹, $zJ' = -0.50 \pm 0.01$ cm⁻¹ and $g = 2.02 \pm 0.01$ for **6**; $J = -3.30 \pm 0.02$ cm⁻¹, $zJ' = -0.36 \pm 0.01$ cm⁻¹ and $g = 2.00 \pm 0.01$ for **7**. The exchange interactions found for **5-7** are in good agreement with the Cr-Mn antiferromagnetic interaction of -4.40 cm⁻¹ reported for a similar system.^[27]

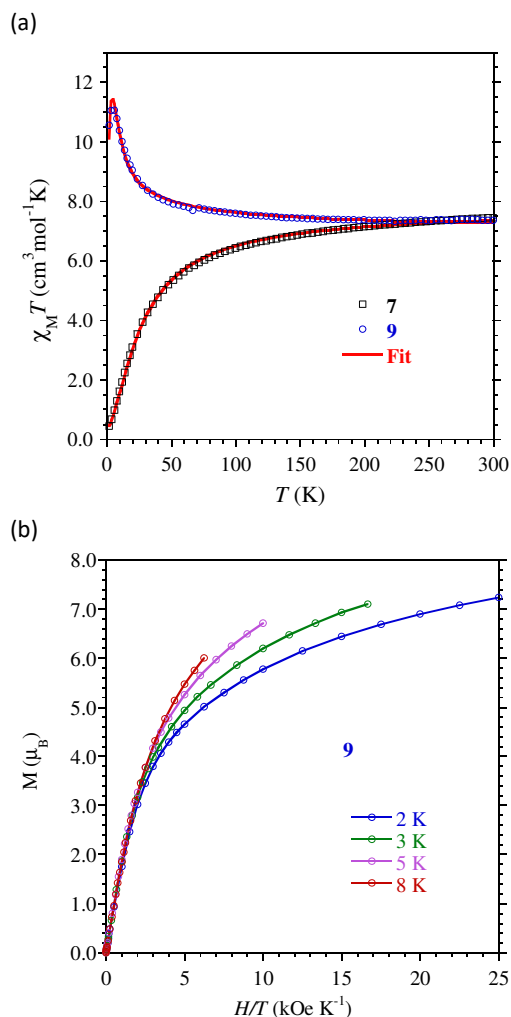


Figure 2. (a) Experimental (O/□) and calculated (—) temperature dependence of $\chi_M T$ for **7** and **9**, the best fit parameters are discussed in the text; (b) M versus H/T for **9** (the lines are just eye guides).

For the $[\text{Cr}_2\text{Fe}]$ species **8** and **9**, the $\chi_M T$ value of 7.16 and 7.35 $\text{cm}^3\text{mol}^{-1}\text{K}$ have been obtained at 300 K; they conform to the Curie contributions of 7.22 $\text{cm}^3\text{mol}^{-1}\text{K}$ anticipated for two Cr^{III} and one high spin Fe^{II} with $g_{\text{Fe}} = 2.15$. For both compounds, the $\chi_M T$ value is hardly changing between 300 and 50 K (Figure 2 and S17) before increasing to a maximum of 9.69 and 11.16 $\text{cm}^3\text{mol}^{-1}\text{K}$ (at 4 and 5 K, respectively), and finally dropping to 9.05 and 10.54 $\text{cm}^3\text{mol}^{-1}\text{K}$ at 2 K. This behavior is characteristic for ferromagnetic Cr-Fe interactions while the low temperature decrease reflects the presence of magnetic anisotropy and possible intermolecular interactions. Magnetic anisotropy is also revealed by the magnetization curves of **8** and **9** (Figure S16) with values reached in high fields much below 10 μ_B and their non-superposition when plotted against H/T (Figure 2b). Attempts to estimate J_{CrFe} , g_{mean} , and D_{Fe} (the axial ZFS parameter of the Fe^{II} center) for these complexes by simultaneous adjustments of $\chi_M T = f(T)$ and $M = f(H)$ data yielded unrealistic D_{Fe} values. The theoretical insights (*vide*

infra) indicate that a good description of the magnetic system requires more parameters to be considered. Nevertheless, a first estimation was obtained modeling the $\chi_{MT} = f(T)$ data, best fit yielded $J = 2.12 \pm 0.01 \text{ cm}^{-1}$, $D_{\text{Fe}} = -11.00 \pm 0.07 \text{ cm}^{-1}$, $zj' = -0.020 \pm 0.001 \text{ cm}^{-1}$ and $g = 2.08$ for **8**; and $J = 2.80 \pm 0.04 \text{ cm}^{-1}$, $D_{\text{Fe}} = -20 \pm 1 \text{ cm}^{-1}$, $zj' = -0.014 \pm 0.001 \text{ cm}^{-1}$ and $g = 2.10$ for **9** (a negative D_{Fe} value was used as first guess). These values well compare with reported $J = 2.05 \text{ cm}^{-1}$, $D_{\text{Fe}} = -25 \text{ cm}^{-1}$, $zj' = -0.015 \text{ cm}^{-1}$ for the $[\text{Cr}_2\text{FeNH}_2]$.^[33] We can notice that the intermolecular contributions (zJ') are noticeably weaker compared to the ones obtained for the Mn analogues, however this parameter was required to reproduce the low temperature maximum (see Figure S17). Because the contributions of zJ' and D_{Fe} to χ_{MT} operate in the same temperature domain (2 – 20 K), these parameters are strongly correlated and the values yielded by the fitting process should be viewed with caution. This is not the case for J , the ferromagnetic Cr-Fe interaction is the only origin for the increase of χ_{MT} below 50 K.

The appearance of slow relaxation of the magnetization for **8** and **9** has been probed by measuring their AC susceptibility below 20 K. An out-of-phase magnetic susceptibility (χ_M'') was observed for **8** but without a maxima whether in zero field or with applied fields (Figure S18). However, **9** showed a well-defined maximum at 3 K (for an AC frequency of 1 kHz, Figure S19-20) in zero field that shifted to higher T when a field was applied. The optimal field was determined to be 1 kOe (Figure S19b). The frequency (1 to 1500 Hz) and temperature-dependence of AC susceptibility was collected at 0 (Figure 3a and Figure S20) and 1 kOe (Figure 3b and Figure S22). The relaxation times, τ , have been deduced from the $\chi_M'' = f(\nu)$ data using the generalized Debye model (Figures SI20d and SI22d),^[40] and their temperature dependence analyzed with the Arrhenius model (Figure 3c and Figure 3d). The best fits gave an energy barrier of $U_{\text{eff}}/k_B = 19 \text{ K}$ with $\tau_0 = 3.5 \cdot 10^{-7} \text{ s}$ in zero field, and $U_{\text{eff}}/k_B = 35.6 \text{ K}$ with $\tau_0 = 6.8 \cdot 10^{-8} \text{ s}$ with an applied static field of 1 kOe. These values similar to those obtained for the related complex $[\text{Cr}_2\text{FeNH}_2]$ ^[33] (Table 1).

To decipher the origin of the discrepancy in SMM behavior for these complexes, theoretical calculations were undertaken to estimate the effective magnetic anisotropy of the metal centers and the Cr-Fe exchange interactions.

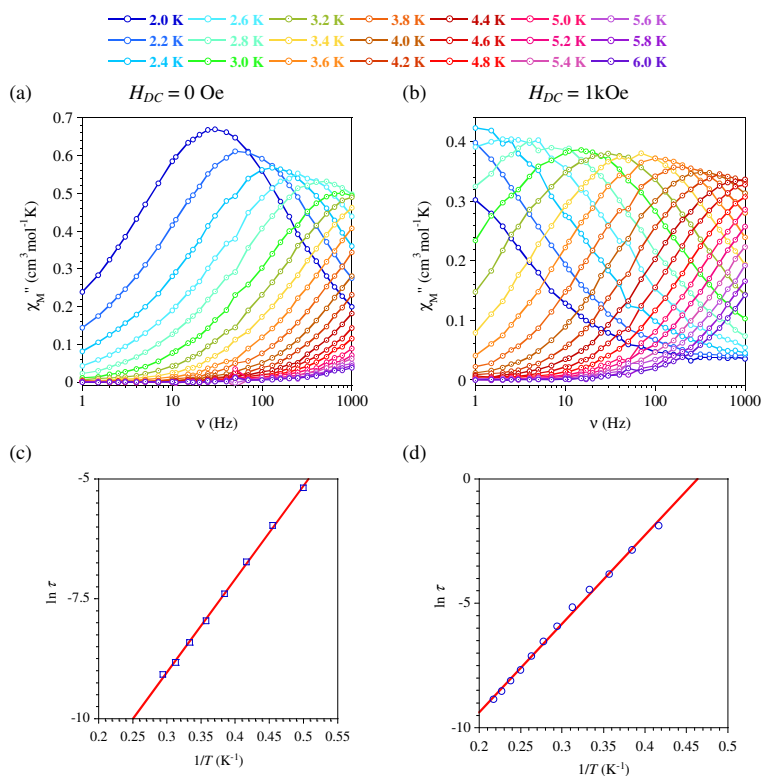


Figure 3. Frequency dependence of the out-of-phase component of the ac susceptibility for **9**, and temperature dependence of the relaxation time (○) with an Arrhenius analysis (—) (a,c) in zero field, (b,d) in applied static field of 1 kOe. The best fit parameters are discussed in the text.

Theoretical calculations:

The values of the magnetic anisotropy parameters of Fe^{II} and Cr^{III} and of the magnetic isotropic coupling between these ions for complexes **8**, **9** and for [Cr₂FeNH₂] are extracted from wave-function based calculations. A zeroth-order description is first obtained using the Complete Active Space Self Consistent (CASSCF) method where the 3d electrons and orbitals are introduced in the active space. Then the N-Electron Valence state Perturbation Theory (NEVPT2)^[41-43] method is used to introduce dynamic correlation. Finally, to determine the anisotropic parameters, the spin-orbit interaction is calculated using the Spin-Orbit State Interaction (RASSISO) method.^[44-46] Isotropic magnetic couplings are extracted from DFT calculations performed on the full trinuclear complexes (see Experimental Section for details).

For [Cr₂FeNH₂] these parameters were re-assessed to allow comparison between the three [Cr₂Fe] derivatives. In complex **8** the two Cr^{III} are crystallographically inequivalent, and **9** is found in two slightly non-equivalent geometrical structures but in which the two Cr^{III} centers

are equivalent. Values are reported in Table 1, the orientation of the magnetic axis is shown in Figure 4. The coordinate frame centered on Fe is as follows: x and y are in the plane of the pentadentate ligand, (x in the direction of the pyridine-N atom), z is pointing toward the apical ligands' atom, *i.e.*, roughly in the direction of the Cr^{3+} ions. In agreement with earlier reports for related complexes, the easy magnetic axis of the Fe^{II} center is aligned along the apical coordination sites.^[24, 33]

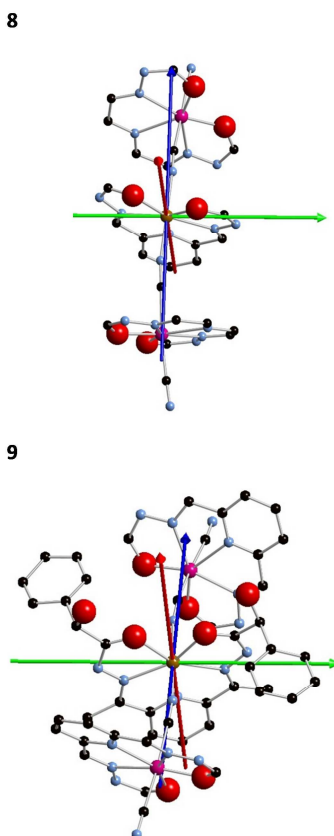


Figure 4. Orientation of the magnetic axes in **8** (top) and **9** (bottom). x in red, y in green and easy magnetic axis z in blue. Cr in purple, Fe in brown, N in blue, O in red and C in black. H atoms are not represented for clarity reasons.

Regarding the Fe^{II} ions, they exhibit in complex **9** quite large D_{Fe} and small E_{Fe} values (-23 cm^{-1} and 1 cm^{-1} , respectively), while in **8** D_{Fe} is much smaller and E_{Fe} larger (-14 cm^{-1} and 2.1 cm^{-1} , respectively), in agreement with the experimental values. The g_{Fe} values are quite similar in both complexes even if the contrasts are larger for **9**. As expected, the anisotropy parameters of the Cr^{III} ions are small, D_{Cr} of about -1 cm^{-1} , E is close to $|D|/3$ and g_{Cr} is almost equal to 2. Noteworthy differences in the exchange interaction between the Fe^{II} and Cr^{III}

centers are found. Indeed, **8** presents the weakest coupling with $J_{\text{FeCr2}} = 1.0 \text{ cm}^{-1}$ and almost zero for J_{FeCr1} , while these couplings are 1.0 cm^{-1} and 2.8 cm^{-1} in $[\text{Cr}_2\text{FeNH}_2]$, and 2.0 cm^{-1} and 1.5 cm^{-1} in **9**. It is satisfying to note that the $M = f(H)$ behaviors calculated with the above sets of parameters show fairly good correspondence with the experimental behaviors for **8** and **9** (Figure SI24).

The outcome of the calculations reveals significant difference both in the magnetic anisotropy of the Fe^{II} centers and in the exchange interactions between the Cr and Fe centers. Since the geometry of the first coordination spheres for the Fe centers is hardly changed in these complexes (Table S1), these alterations in D_{Fe} and J_{CrFe} must be attributed to the deformation of Fe-CN linkages. The structural information for the complexes indicates a tilt with respect to a straight Fe–N≡C bonding normal to the pentagonal plane, which is smallest for **9** (11.8° , mean value) and largest for **8** (19.6°) while $[\text{Cr}_2\text{FeNH}_2]$ exhibits an intermediate deviation (16.1°).

To reach a better understanding on the impact of the tilt of M–N≡C linkage on the D_{Fe} value, additional calculations on model complexes have been performed. The pentadentate ligand around the Fe^{2+} ion was simplified by replacing the R-groups by H atoms and the structure was symmetrized to a C_{2v} point group (coordinates are given in table SI12). In the most symmetric complex, used as a reference, both CN^- ligands are perpendicular to the plane defined by the equatorial coordination sites. Then, the orientation of the two CN^- ligands with the pentagonal plane was varied (Figure 5) while the Fe–N distance was fixed to 2.11 \AA .

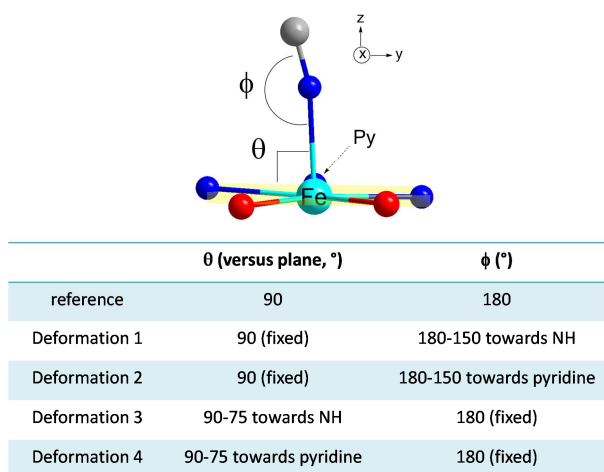


Figure 5. Angular deformations applied to the apical CN-ligands in the model complex

In the two first series (Table 2), the Fe–N–C angle ϕ varies from 180° to 150° while all N'–Fe–N angles θ (N' is one of the hydrazone nitrogen) remain equal to 90° . In the first series, the

CN-ligands are bent towards the hydrazone nitrogen while in the second it is bent towards the pyridine nitrogen. In the third and fourth series, ϕ angles are 180° while θ is varied from 90° to 75° , towards the hydrazone nitrogen for the third series and towards the pyridine nitrogen in the fourth one. Results are reported in Table 2.

It can be observed that for the most symmetric model d_{xz} and d_{yz} (as $d_{x^2-y^2}$ and d_{xy}) are close in energy but not degenerate since the model pentadentate ligand does not present a C_5 -symmetry axis. This lift of degeneracy indicates that the ligand field effect of the pentadentate ligand is slightly smaller in the direction of the pyridine N atom. As a consequence, the ground state essentially carried by the configuration $(d_{yz})^2 d_{xz} d_{x^2-y^2} d_{xy} d_{z^2}$ is not degenerate and the energy of the first excited state (mainly $d_{yz} (d_{xz})^2 d_{x^2-y^2} d_{xy} d_{z^2}$) is about 400 cm^{-1} higher (MOs are shown in Figure SI25). The main contribution (nearly -20 cm^{-1}) to D arises from the spin-orbit coupling between the ground state and the first excited quintet state, while the contributions of the three other quintets are positive and much smaller, reaching a maximum of $+4 \text{ cm}^{-1}$ in total. As the various deformations hardly affect the contributions of these last three quintets, the discussion will focus on the first excited quintet state. It must also be noted that for some deformations we observe a drastic change of the magnetic anisotropy, *i.e.* the axes x and z are exchanged and the contributions of the first excited states become positive. Since a fine analysis of this qualitative change would not bring any relevant information for the understanding of the studied complexes, these contributions are not reported in Table 2.

The bending of the Fe-N-C linkage towards the hydrazone-N atom (Def. 1) leads to larger negative values of D while magnetic anisotropy is slightly reduced when bending towards the pyridine moiety. The variation of the θ -angle has a more significant effect on D that decreases in absolute value and even turns positive as the angle deviates from 90° . These trends can be directly related to the evolution of the gap between the ground and first excited quintet states which can also be correlated with the energy of the *ab initio* ligand field theory (AILFT)^[47] Fe^{2+} MOs given in Table 2. Indeed, the energy gap is inversely proportional to the contributions to D (according to the second-order perturbation theory) and is all the larger as the energy difference between the orbitals involved in the excitation is important.

Table 2. Variation of D with the deformation of the apical C-N-Fe linkage (see text), energy of AILFT MO, energy of the five quintet states (Q_0 is the ground state, Q_{1-4} are the first, second, third, and fourth excited states) and contributions of these excited states to the total D value. Positive contributions to D arising from the first excited quintet state are not reported (see text).

structures		$D / E \text{ cm}^{-1}$	AILFT MO energy					Quintet state energy / Contribution to D				
			d_{xz}	d_{yz}	$d_{x^2-y^2}$	d_{xy}	d_{z^2}	Q_0	Q_1	Q_2	Q_3	Q_4
$\theta = 90, \phi = 180$		-15.3/2.2	0	277	2413	3611	9560	0	409 -20.3	3405 +1.4	4975 +1.1	12122 +1.4
Def. 1	$\phi=170^\circ$	-16.0/2.2	0	264	2415	3601	9500	0	387 -21.1	3396 +1.4	4963 +1.1	12028 +1.4
	$\phi=160^\circ$	-18.0/2.0	0	235	2411	3574	9328	0	335 -23.2	3364 +1.4	4929 +1.1	11764 +1.4
	$\phi=150^\circ$	-20.7/1.7	0	197	2400	3542	9058	0	272 -26.0	3321 +1.4	4884 +1.1	11364 +1.5
Def. 2	$\phi=170^\circ$	-15.0/2.2	0	284	2433	3613	9509	0	418 -20.0	3425 +1.4	4985 +1.1	12045 +1.4
	$\phi=160^\circ$	-13.4/2.4	0	318	2469	3620	9370	0	471 -18.4	3458 +1.3	5007 +1.1	11836 +1.4
	$\phi=150^\circ$	-11.2/2.5	0	375	2512	3638	9148	0	560 -16.2	3500 +1.3	5038 +1.0	11513 +1.5
Def. 3	$\theta=85^\circ$	-15.1/2.1	0	263	2392	3563	9407	0	414 -20.2	3367 +1.4	4934 +1.1	11933 +1.4
	$\theta=80^\circ$	-11.5/1.6	0	367	2395	3532	9033	0	538 -16.7	335 +1.5	4920 +1.0	11480 +1.4
	$\theta=75^\circ$	+5.6/1.7	0	724	2475	3623	8497	0	944	3455 +1.3	5015 +1.1	10874 +1.4
Def. 4	$\theta=85^\circ$	-9.9/2.6	0	428	2462	3630	9476	0	624 -14.8	3449 +1.3	5010 +1.1	12015 +1.4
	$\theta=80^\circ$	+6.7 1.0	0	737	2546	3703	9192	0	1036	3551 +1.3	5103 +1.1	11683 +1.4
	$\theta=75^\circ$	+5.2 0.7	0	1184	2650	3835	8687	0	1611	3705 +1.3	5251 +1.1	11147 +1.4

The angular distortions in the real species **8** and **9** combine the θ and ϕ deformations applied to the model complex and Table 2 can be used to rationalize their relative D value. For **9**, the two Fe-NC linkages are bent with $\phi = 169.7$ and 166.7° towards a hydrazine-N atom, a situation leading to large negative D values (Def 1 in Table 2) while $\theta = 86.2$ and 86.5° , also towards the hydrazine, are in the range of values for which large negative contributions still apply (Def. 3). For **8**, one Fe-NC is bent in an intermediate direction between the pyridine- and a hydrazone-N atoms with $\phi = 167^\circ$, leading to a large negative contribution, but $\theta = 87.2/87.5^\circ$ should induce a much smaller negative contribution due to the partial orientation towards the pyridine. The second CN⁻ is bent towards the pyridine unit with $\phi = 163.5^\circ$ and $\theta = 88.5^\circ$, which should induce a much smaller negative D value (Def. 2 and 4). In summary, it is the orientation of the CN⁻ in the vicinity of the Fe^{II} ion which conditions the relative values of D in these complexes and rationalizes the obtaining of a more negative D value for **9** than for **8**, in agreement with both the *ab initio* results and the experimental magnetic behaviors (Table 1).

The π -orbitals of the CN-ligands are also the pathways for the exchange interactions between the metal centers. The orthogonality of the magnetic t_{2g} orbitals of Cr and the singly-occupied d_{xy} , $d_{x^2-y^2}$, and d_{z^2} orbitals of Fe^{II} contributes to a ferromagnetic interaction while the remaining pathway with $d_{xz/yy}$ is antiferromagnetic.^[9] When the Cr-CN-Fe linkage is normal to the equatorial plane (i.e. $\theta = 90^\circ$ and $\phi = 180^\circ$, Figure 5), the ferromagnetic contribution is larger and the observed Fe-Cr interaction is ferromagnetic. As soon as θ deviates from 90° the antiferromagnetic contribution is increased, resulting in a lower effective ferromagnetic Fe-Cr interaction. This is precisely the trend obtained if the J_{CrFe} values obtained by DFT are compared with respect to the deviation from the normal to pentagonal plane of the direction of the C-N axis of the ligand connecting Fe and Cr (Table 1). The ferromagnetic interaction, J_{CrFe} , is largest (2.8 cm^{-1}) for smallest deviation (6.1°) and decreases for larger deviations. The same trend is followed by the experimental J_{CrFe} values found for the complexes.

The information provided by the calculations allows understanding the different demagnetization dynamics observed for these [Cr₂Fe] complexes. For **9**, large magnetic anisotropy of Fe^{II} combined with stronger ferromagnetic interactions stabilizing the $S = 5$ ground spin state contribute to SMM behavior with highest energy barrier for magnetization reversal. In comparison, **8** has significantly smaller anisotropy and weakly exchange coupled

magnetic centers, accounting for the absence of SMM behavior above 2 K. The situation for [Cr₂FeNH₂] is intermediate, consequently $U_{\text{eff}}/k_{\text{B}}$ was found slightly smaller than for **9**.

CONCLUDING REMARKS

The incidence of the twisting of the cyanide coordination on the anisotropy of metal ion is certainly an effect that is usually considered as negligible; the results gathered here show that this is not always the case. For the Fe^{II} derivatives concerned by our study, this effect translated into significant differences in SMM behaviors of otherwise very similar compounds. It must be concluded that it is preferable to achieve coordination perpendicular to the equatorial plane of the PBP Fe center to reach largest $|D_{\text{Fe}}|$ and, consequently SMMs with higher energy barriers for magnetization reversal. An illustration is given by the trinuclear [Cr₂Fe] complex with a deviation of the Fe-N≡C linkages of about 10° from normal to plan for which SMM behavior with $U_{\text{eff}}/k_{\text{B}} = 35$ K was achieved, while for its homologue with a bending of about 20° only an onset of slow relaxation was found above 2 K.

It is very likely that a dependence of the magnetic anisotropy on the deviation from linearity of the M-NC linkage applies also for other coordination geometries. This would explain the strong differences in SMM behavior often found for otherwise very similar compounds.

A control of the deformation of this linkage can be achieved by the design of the molecular building blocks. In the reported derivatives, substituents with increased steric demand in the space between the adjacent molecular units enforced a straighter linkage in the apical positions of the pentagonal bipyramid Fe unit, thus contributed to larger magnetic anisotropy.

EXPERIMENTAL SECTION.

Materials and methods: All reagents and solvents were used as received from commercial sources unless otherwise specified. The organic derivatives cyclohexanecarbohydrazine,^[48] H₂L^{N³O²NH₂},^[49] (*S*)-2-hydroxy-2-phenylacetohydrazide abbreviated *S*-mandCONHNH₂,^[50] the complexes [MnL^{N³O²NH₂}(H₂O)Cl]Cl·2H₂O^[51] and K[Cr(L^{N³O²Ph})(CN)₂]·2H₂O^[27] were synthesized following published synthetic procedures, while that for [Mn(H₂L^{N³O²mand})Cl₂] and [Fe(H₂L^{N³O²mand})Cl₂] complexes were adapted from the synthesis of other divalent metal complexes (see below for the experimental details)^[52]. All the syntheses of Fe^{II} complexes were carried out under N₂ using Schlenk techniques using degassed solvents (diethyl ether

purified using an Innovative Technology Solvent Purification® system while the alcohol and water solvents were distilled under N₂ prior to use); the solid samples for the characterizations were prepared in a glovebox. Fourier transform infrared (FT-IR) spectroscopy was performed with a Perkin–Elmer spectrum GX 2000 FT-IR spectrometer. Elemental analyses were performed with a Perkin–Elmer 2400 series II instrument. Magnetic studies were carried out with a Quantum Design MPMS-5S SQUID magnetometer on freshly isolated polycrystalline powders put in gelatin capsules (for [Cr₂Mn] complexes) or in quartz tubes (for [Cr₂Fe] derivatives) mixed to grease. Data have been collected between 300 and 2 K with an applied field of 1 kOe and corrected for the diamagnetic contribution sample by using Pascal's tables^[53] and for the sample holder. The field dependences of the magnetization were measured between 2 and 8 K with dc magnetic field up to 5 T. The absence of ferromagnetic impurities was checked by measurement of *M* vs. *H* at 100 K.

Powder X-Ray diffraction (PXRD) data were collected on a XPert Pro (*Theta–Theta* mode) Panalytical diffractometer in transmission mode using capillary tubes with $\lambda(\text{CuK}_{\alpha 1}, \text{K}_{\alpha 2}) = 1.54059$ and 1.54439 \AA .

Syntheses:

*H*₂*L*^{N3O2cyclohex}: Cyclohexanecarbohydrazide (2.2 g, 15.5 mmol) was dissolved in 100 mL EtOH 96 % acidified with one drop of concentrated HCl (37 %). 2,6-diacetylpyridine (1.148 g, 7.03 mmol) was added under stirring. A white precipitate appeared after 5 minutes. The suspension was refluxed for 3 hours then allowed to cool in an ice bath. The off-white powder was filtered, washed several times with cold EtOH and vacuum dried. Yield : 2.86 g (99 %). ¹H NMR (400 MHz, d⁶-DMSO in the presence of ZnCl₂, see SI) δ : 12.50 (s, 2 H, NH), 8.32 (t, 1 H, ArH), 8.16 (d, 2 H, ArH), 2.71-2.64 (tt, 2 H, CH_{cyclo}), 2.56 (s, 6 H, CH₃), 1.89-1.20 (m, 20 H, CH_{2 cyclo}) ppm; ¹³C NMR (75 MHz, CDCl₃) δ : 177.1, 147.8, 146.8, 143.1, 124.7, 42.1, 29.1, 25.5, 25.4, 13.6 ppm.

[Mn(*H*₂*L*^{N3O2cyclohex})Cl₂].0.5H₂O, **1**: *H*₂*L*^{N3O2cyclohex} (200 mg, 0.49 mmol) was suspended in 6 mL of absolute EtOH and warmed at 40°C in an one-necked flask. A solution of MnCl₂.4H₂O (100 mg, 0.5 mmol, 6 mL absolute EtOH) was then added and the mixture was refluxed for 2 hours, cooled to room temperature and precipitated by addition into cold pentane. The yellow powder was dried in an oven at 60°C for one night. Yield: 252 mg (94 %). IR (ATR diamond, cm⁻¹): 3103 (w), 3069 (w), 2930 (m), 2855 (m), 1660 (s), 1641 (m), 1521 (m), 1448 (w), 1381

(w), 1334 (w), 1312 (m), 1265 (w), 1247 (m), 1201 (s), 1177 (s), 1134 (w), 1106 (w), 1085 (w), 1010 (w), 994 (w), 956 (w), 895 (w), 876 (sh), 820 (m), 813 (w), 777 (w), 749 (w), 724 (w), 696 (m), 648 (m), 545 (w), 518 (w). Elemental analysis (%) calcd. for $C_{23}H_{34}Cl_2MnN_5O_{2.5}$ ($[Mn(H_2L^{N3O2cyclohex})Cl_2] \cdot 0.5H_2O$): C 50.56; H 6.27; N 12.82; found: C 50.73; H 6.31; N 12.69.

$[Mn(H_2L^{N3O2mand})Cl_2] \cdot 2H_2O$, **2**: 2,6-diacetylpyridine (326 mg, 2 mmol) and *S*-mandCONHNH₂ (670 mg, 4 mmol) were mixed in 30 mL of ethanol with 1 drop of H₂SO₄. The white suspension was refluxed for 1 day and cooled to room temperature. MnCl₂·4H₂O (396 mg, 2 mmol) dissolved in 10 mL EtOH was added at room temperature to the reaction mixture. The mixture was refluxed for 2 additional hours affording a yellow solution. The solution was settled for crystallization at room temperature yielding long and fine needles after 4 days of evaporation. Yield: 1.03 g (83 %). IR (KBr, cm⁻¹): 3382 (m), 3093 (m), 3033 (m), 3002 (m), 2960 (m), 2921 (m), 2879 (m), 1655 (s), 1641(sh), 1590 (w), 1531 (m), 1502 (sh), 1456 (w), 1439 (w), 1383 (m), 1333 (w), 1318 (w), 1266 (m), 1260 (sh), 1209 (m), 1171 (m), 1086 (m), 1060 (m), 1038 (m), 1026 (m), 1015 (m), 972 (w), 921 (w), 852 (w), 821 (m), 812 (sh), 767 (w), 737 (w), 728 (m), 698 (m), 659 (m), 641 (m), 609 (w), 565 (m), 535 (m), 508 (w). Elemental analysis (%) calcd. for $C_{25}H_{28}Cl_2MnN_5O_{5.5}$ ($[Mn(H_2L^{N3O2mand})Cl_2] \cdot 2H_2O$): C 48.73; H 4.58; N 11.37; found: C 48.75; H 4.39; N 11.59.

$[Fe(H_2L^{N3O2cyclohex})Cl_2] \cdot 2MeOH$, **3**: H₂L^{N3O2cyclohex} (184 mg, 0.45 mmol) and FeCl₂·4H₂O (89 mg, 0.45 mmol) were dissolved in 6 mL MeOH and the dark blue violet solution was mixed for 1 night at room temperature. Diethyl ether (30 mL) was added into the solution allowing the complex to precipitate. Yield: 210 mg (93 %). IR (ATR diamond, cm⁻¹): 3162 (w), 3080 (m), 3000 (m), 2928 (vs), 2856 (m), 2792 (w), 1633 (s), 1526 (s), 1449 (m), 1397 (w), 1378 (w), 1336 (w), 1320 (sh), 1268 (w), 1257 (w), 1203 (m), 1177 (m), 1136 (w), 1086 (w), 1018 (m), 996 (sh), 955 (w), 894 (w), 810 (m), 779 (w), 738 (w), 666 (b). Elemental analysis (%) calcd. for $C_{25}H_{41}Cl_2FeN_5O_4$ ($[Fe(H_2L^{N3O2cyclohex})Cl_2] \cdot 2MeOH$): C 49.85; H 6.86; N 11.63; found: C 49.59; H 6.90; N 11.61.

$[Fe(H_2L^{N3O2mand})Cl_2] \cdot 2H_2O$, **4**: 2,6-diacetylpyridine (228 mg, 1.4 mmol) and *S*-mandCONHNH₂ (465 mg, 2.8 mmol) were mixed in 20 mL of methanol. The white

suspension was refluxed for 1 day. FeCl₂·4H₂O (280 mg, 1.4 mmol) was added solid after bringing back the solution at room temperature. The mixture was stirred at room temperature overnight affording a dark blue violet solution. Diethyl ether (30 mL) was added on top to precipitate the product as a blue violet powder. Yield: 0.75 g (78 %). IR (ATR diamond, cm⁻¹): 3252 (br), 3086 (m), 2908 (m), 2824 (m), 2735 (m), 1651 (s), 1642 (sh), 1598 (w), 1531 (m), 1494 (sh), 1456 (w), 1429 (w), 1381 (w), 1333 (w), 1318 (w), 1268 (m), 1239 (m), 1217 (s), 1186 (m), 1167 (m), 1086 (s), 1064 (m), 1017 (s), 972 (w), 920 (w), 856 (w), 828 (m), 807 (m), 766 (m), 734 (w), 698 (s), 673 (m), 659 (sh), 602 (m), 543 (w), 509 (m). Elemental analysis (%) calcd. for C₂₅H₃₅Cl₂FeN₅O_{8.5} ([Fe(H₂L^{N3O2mand})Cl₂].4.5H₂O): C 45.00; H 5.13; N 10.49; found: C 45.08; H 5.04; N 10.54.

[[Cr(L^{N3O2Ph})(CN)₂]₂Mn(H₂L^{N3O2NH2})]·5MeOH, 5: [Mn(H₂L^{N3O2NH2})Cl₂] (0.030 g, 0.07 mmol) in 2 mL MeOH and 2 mL H₂O was added dropwise to a solution of K[Cr(L^{N3O2Ph})(CN)₂] (0.080 g, 0.15 mmol) in 12 mL MeOH. An orange solid slowly appeared during the addition. The suspension was stirred overnight at room temperature. The solid was filtered and washed with 1-2 mL of a mixture H₂O/MeOH 50:50 followed by Et₂O (5 mL), yielding 55 mg (55 % based on Cr) of **5**. Phase purity of this polycrystalline solid was confirmed by PXRD, see Figure S3. Conditions to grow single crystals suitable for X-ray data collection: A solution of K[Cr(L^{N3O2Ph})(CN)₂].2H₂O (0.021 g, 0.04 mmol) in 3 mL MeOH was placed in a 1 cm diameter tube and layered with 2 mL of MeOH. [Mn(H₂L^{N3O2NH2})Cl₂] (0.008 g, 0.02 mmol) dissolved in H₂O/MeOH 50:50 (1 mL) was slowly layered on the top. Good quality crystals were isolated after 1 night. IR (KBr, cm⁻¹): 2153 (w), 2128 (w), 1671 (s), 1652 (m), 1585 (m), 1559 (sh), 1517 (s), 1504 (sh), 1432 (w), 1380 (s), 1343 (sh), 1306 (m), 1269 (m), 1187 (m), 1174 (w), 1093 (m), 1069 (m), 1045 (m), 1026 (m), 1011 (m), 993 (w), 932 (w), 905(w), 808 (w), 759 (w), 737 (w), 713 (m), 682 (m). Elemental analysis (%) calcd. for C₆₃H₆₁Cr₂MnN₂₁O₈ ([{Cr(L^{N3O2Ph})(CN)₂]₂Mn(H₂L^{N3O2NH2})]·2MeOH): C 54.08; H 4.39; N 21.02; found: C 53.97; H 4.31; N 20.97.

[[Cr(L^{N3O2Ph})(CN)₂]₂Mn(H₂L^{N3O2cyclohex})]·5H₂O·2.5MeOH, 6: [Mn(H₂L^{N3O2cyclohex})Cl₂] (0.030 g, 0.06 mmol) in 17 mL MeOH was added dropwise to a solution of K[Cr(L^{N3O2Ph})(CN)₂].2H₂O (0.063 g, 0.11 mmol) in 12 mL H₂O. An orange solid slowly appeared during the addition. The suspension was stirred overnight at room temperature. The solid was filtered and washed with 1-2 mL of a mixture H₂O/MeOH 50:50 followed by Et₂O

(5 mL), yielding 45 mg (50 % based on Cr) of **6**. Phase purity of this polycrystalline solid was confirmed by PXRD, see Figure S6. Conditions to grow single crystals suitable for X-ray data collection: A solution of $[\text{Mn}(\text{H}_2\text{L}^{\text{N}3\text{O}2\text{cyclohex}})\text{Cl}_2]\cdot 0.5\text{H}_2\text{O}$ (0.07 g, 0.01 mmol) dissolved in H_2O (3 mL) was placed in a 1 cm diameter tube and layered with 2 mL of $\text{H}_2\text{O}/\text{MeOH}$ 50:50. $\text{K}[\text{Cr}(\text{L}^{\text{N}3\text{O}2\text{Ph}})(\text{CN})_2]\cdot 2\text{H}_2\text{O}$ (0.015 g, 0.03 mmol) in 4 mL MeOH was slowly layered on the top. Single crystals suitable for X-ray data collection were isolated after 4 days. Yield: 7.1 mg (33 %). IR (KBr, cm^{-1}): 2925 (m), 2853 (m), 2159 (w), 2133 (w), 1654 (m), 1652 (m), 1586 (m), 1555 (m), 1516 (s), 1434 (w), 1450 (w), 1418 (m), 1381 (s), 1339 (w), 1306 (sh), 1283 (w), 1253 (w), 1200 (w), 1176 (m), 1071 (w), 1047 (m), 1027 (w), 993 (w), 905 (w), 807 (w), 738 (w), 712 (m), 683 (m). Elemental analysis (%) calcd. for $\text{C}_{73}\text{H}_{81}\text{Cr}_2\text{MnN}_{19}\text{O}_{11}$ ($[\{\text{Cr}(\text{L}^{\text{N}3\text{O}2\text{Ph}})(\text{CN})_2\}_2\text{Mn}(\text{H}_2\text{L}^{\text{N}3\text{O}2\text{cyclohex}})]\cdot 5\text{H}_2\text{O}$): C, 56.22; H, 5.24; N, 17.07; found: C, 56.46; H, 5.24; N, 16.64.

$[\{\text{Cr}(\text{L}^{\text{N}3\text{O}2\text{Ph}})(\text{CN})_2\}_2\text{Mn}(\text{H}_2\text{L}^{\text{N}3\text{O}2\text{mand}})]\cdot 13\text{H}_2\text{O}$, **7**: $[\text{Mn}(\text{H}_2\text{L}^{\text{N}3\text{O}2\text{mand}})\text{Cl}_2]\cdot 2\text{H}_2\text{O}$ (0.024 g, 0.04 mmol) in 4 mL H_2O was added dropwise to a solution of $\text{K}[\text{Cr}(\text{L}^{\text{N}3\text{O}2\text{Ph}})(\text{CN})_2]\cdot 2\text{H}_2\text{O}$ (0.044 g, 0.08 mmol) in 8 mL H_2O . An orange solid slowly appeared during the addition. The suspension was stirred overnight at room temperature. The solid was filtered and washed with 1-2 mL of MeOH followed by Et_2O (5 mL), yielding 35 mg (52 % based on Cr) of **6**. Phase purity of this polycrystalline solid was confirmed by PXRD, see Figure S7. Conditions to grow single crystals suitable for X-ray data collection: A solution of $[\text{Mn}(\text{H}_2\text{L}^{\text{N}3\text{O}2\text{mand}})\text{Cl}_2]\cdot 2\text{H}_2\text{O}$ (0.006 g, 0.01 mmol) dissolved in H_2O (1 mL) was placed in a 1 cm diameter tube and layered with 2 mL of H_2O . $\text{K}[\text{Cr}(\text{L}^{\text{N}3\text{O}2\text{Ph}})(\text{CN})_2]\cdot 2\text{H}_2\text{O}$ (0.011 g, 0.02 mmol) in 2 mL H_2O with 0.2 mL MeOH was slowly layered on the top. Single crystals suitable for X-ray data collection were isolated after 1 night. IR (KBr, cm^{-1}): 2147 (w), 2138 (w), 1673 (m), 1652 (m), 1639 (m), 1586 (m), 1559 (m), 1516 (s), 1494 (sh), 1455 (w), 1428 (m), 1384 (s), 1341 (w), 1306 (w), 1291 (w), 1278 (w), 1201 (w), 1172 (m), 1161 (sh), 1088 (w), 1071 (w), 1045 (m), 1024 (m), 994 (w), 942 (w), 938 (w), 905 (w), 854 (w), 811 (w), 802 (sh), 736 (w), 716 (m), 683 (m). Elemental analysis (%) calcd. for $\text{C}_{75}\text{H}_{89}\text{Cr}_2\text{MnN}_{19}\text{O}_{21}$ ($[\{\text{Cr}(\text{L}^{\text{N}3\text{O}2\text{Ph}})(\text{CN})_2\}_2\text{Mn}(\text{H}_2\text{L}^{\text{N}3\text{O}2\text{mand}})]\cdot 13\text{H}_2\text{O}$): C 51.43; H 5.12; N 15.19; found: C 51.54; H 4.98; N 15.12.

$[[Cr(L^{N3O2Ph})(CN)_2]_2Fe(H_2L^{N3O2cyclohex})] \cdot 7H_2O \cdot 2EtOH$, **8**: $K[Cr(L^{N3O2Ph})(CN)_2] \cdot 2H_2O$ (0.164 g, 0.28 mmol) dissolved in 27 mL H_2O was placed in a Schlenk tube (diameter of 4 cm) and layered with 4 mL of $H_2O/EtOH$ 50:50. A solution of $[Fe(H_2L^{N3O2cyclohex})Cl_2] \cdot 2MeOH$ (0.082 g, 0.14 mmol) in $EtOH$ (14 mL) was slowly layered on the top. The interface was turbid at the end of addition. After 2 days, some solid is present at bottom and some crystals are visible at the interface. The diffusion and precipitation were accelerated after 5 days moving delicately the schlenk. Red crystals appeared within 1 night by complete crystallization of the precipitate. The crystals were collected by filtration and washed with $EtOH$ (3 mL) followed by Et_2O (5 mL), yielding 160 mg (76 % based on Fe) of **8**. Phase purity of this polycrystalline solid was confirmed by PXRD, see Figure S9. Conditions to grow single crystals suitable for X-ray data collection: $K[Cr(L^{N3O2Ph})(CN)_2] \cdot 2H_2O$ (0.030 g, 0.06 mmol) dissolved in 6 mL H_2O was placed in a 1 cm diameter tube and layered with 1 mL of $H_2O/EtOH$ 50:50. A solution of $[Fe(H_2L^{N3O2cyclohex})Cl_2]$ (0.032 g, 0.053 mmol) in $EtOH$ (6 mL) was slowly layered on the top. Single crystals suitable for X-ray data collection were isolated after 8 days. Yield: 8 mg (36 %). IR (KBr, cm^{-1}): 2964 (m), 2928 (m), 2855 (m), 2156 (sh), 2141 (w), 1643 (m), 1635 (sh), 1586 (m), 1557 (m), 1516 (s), 1493 (m), 1451 (w), 1430 (w), 1418 (m), 1380 (s), 1340 (m), 1304 (w), 1262 (m), 1202 (m), 1172 (m), 1138 (w), 1100 (w), 1072 (w), 1039 (m), 993 (m), 954 (w), 936 (w), 906 (w), 805 (s), 737 (w), 712 (m), 683 (m), 581 (w), 545 (w). Elemental analysis (%): calcd. for $C_{73}H_{85}Cr_2FeN_{19}O_{13}$ ($[[Cr(L^{N3O2Ph})(CN)_2]_2Fe(H_2L^{N3O2cyclohex})] \cdot 7H_2O$): C 54.92; H 5.37; N 16.67; found: C 54.83; H 5.11; N 16.30.

$[[Cr(L^{N3O2Ph})(CN)_2]_2Fe(H_2L^{N3O2mand})] \cdot 16H_2O$, **9**: $K[Cr(L^{N3O2Ph})(CN)_2] \cdot 2H_2O$ (0.090 g, 0.16 mmol) dissolved in 18 mL H_2O was placed in a 1 cm diameter tube and layered with 4 mL of H_2O . A solution of $[Fe(H_2L^{N3O2mand})Cl_2] \cdot 2H_2O$ (0.052 g, 0.08 mmol) in H_2O (18 mL) was slowly layered on the top. The interface was turbid at the end of addition. After 2 days, some solid is present at bottom and some crystals are visible at the interface. The diffusion and precipitation were accelerated after 2 days moving delicately the schlenk. Red crystals appeared within 2 days by complete crystallization of the precipitate. The crystals were collected by filtration and washed with H_2O (3 mL) followed by Et_2O (5 mL), yielding 79 mg (57 % based on Fe) of **9**. Phase purity of this polycrystalline solid was confirmed by PXRD, see Figure S12. Conditions to grow single crystals suitable for X-ray data collection: A blue violet solution of $[Fe(H_2L^{N3O2mand})Cl_2] \cdot 2H_2O$ (6 mg, 0.009 mmol) in H_2O (2 mL) was placed

in a 1 cm diameter tube and layered with 2 mL of H₂O. K[Cr(L^{N3O2Ph})(CN)₂].2H₂O (10 mg, 0.017 mmol) dissolved in 2 mL H₂O with 0.2 mL MeOH was slowly layered on the top. Single crystals suitable for X-ray data collection were isolated after 2 days. Yield: 5.5 mg (34 %). IR (KBr, cm⁻¹): 3401 (br), 2962 (m), 2920 (m), 2850 (m), 2141 (sh), 2135 (w), 1653 (m), 1635 (sh), 1586 (m), 1558 (m), 1517 (s), 1494 (m), 1457 (w), 1424 (m), 1384 (s), 1340 (m), 1304 (w), 1264 (m), 1172 (m), 1159 (m), 1088 (w), 1071 (w), 1044 (m), 1029 (w), 994 (m), 901 (w), 807 (m), 736 (w), 714 (m), 684 (m), 583 (w), 546 (w). Elemental analysis (%) calcd. for C₇₅H₈₃Cr₂FeN₁₉O₁₈ ([{Cr(L^{N3O2Ph})(CN)₂}₂Fe(H₂L^{N3O2mand})]·10H₂O): C 53.04; H 4.93; N 15.67; found: C 53.23; H 4.63; N 15.49.

Wave Function Theory Calculations:

X-ray diffraction structures were used in all calculations, except for the position of H atoms that was optimized in DFT (PBE^[54] with D3 correction and def2-SVP atomic basis sets for all atoms).

The magnetic anisotropy parameters *D*, *E* and *g* of the Fe^{II} and Cr^{III} ions in the trinuclear complex were extracted from calculations on simplified molecules. For the calculation of the anisotropy of Fe^{II}, the H₂L^{N3O2NH2} and all the CN⁻ ligands are explicitly considered, while the phenyl groups of L^{N3O2Ph} are replaced by H atoms and the Cr³⁺ ions are replaced by Sc³⁺ (same charge but diamagnetic). A similar strategy is used for the calculation of the anisotropy of each Cr^{III}: a given Cr³⁺ ion and the ligands to which it is coordinated are explicitly considered; the Fe²⁺ is replaced by a Zn²⁺ ions (same charge but diamagnetic), its CN⁻ ligands are explicitly considered while its H₂L^{N3O2R} ligand is simplified taking R = H; the second Cr^{III}, its ligand and its external CN⁻ ligand are not considered. For Fe complexes, the active space consists of six electrons in five 3d orbitals, *i.e.* CAS(6/5). All the 5 spin quintet (*S* = 2) and 45 spin triplet (*S* = 1) states generated by the CAS(6/5) are calculated, providing a state average molecular orbitals (MOs) set. Then, dynamic correlations are introduced using the NEVPT2^[41-43] method that brings second-order perturbative correction to the energies. Finally, the magnetic anisotropy parameters of the Fe center are extracted from RASSISO calculations^[44-46] using CASSCF wave functions and NEVPT2 energies. An equivalent procedure is followed for the evaluation of the magnetic anisotropy parameters of Cr^{III} ions but in this case a CAS(3/5) is considered and 10 quartet (*S* = 3/2) and 40 doublet (*S* = 1/2) states are calculated. def2-TZVPP atomic basis sets are used for Fe or Cr (*i.e.* 10s7p4d2f1g), def2-TZVPP for the atoms coordinated to Fe or Cr and for CN⁻ ligands (*i.e.* 6s3p2d1f) and

def2-SVP for other atoms (*i.e.* 5s3p2d1f for Sc or Zn, 3s2p1d for C, N, or O and 2s1p for H), recontracted using the scalar relativistic Douglas-Kroll-Hess Hamiltonian (DKH2).^[55] Calculations were also performed on a series model complexes to emphasize the role of the position of the CN⁻ ligands around the Fe^{II} ion on its *D* and *E* values.

The isotropic magnetic couplings are evaluated from DFT calculations (wB97X-D3 functional)^[56] on the full trinuclear complexes. def2-TZVP atomic basis sets are used for all atoms except H that were described with def2-SV(P) ones.

All WFT and DFT calculations were performed using the ORCA 4.0.0 package.^[57]

Single-crystal X-ray diffraction: Single crystals suitable for X-ray diffraction were coated with paratone oil and mounted onto the goniometer. The X-ray crystallographic data were obtained at low temperature from an Apex2 Bruker diffractometer (MoK α radiation source), equipped with an Oxford Cryosystem. The structures have been solved by direct methods using Shelxs or Superflip and refined by means of least-square procedures on *F* or *F*² using the PC version of the program CRYSTALS.^[58] The scattering factors for all the atoms were used as listed in the International Tables for X-ray Crystallography.^[59] Absorption correction was performed using a multi-scan procedure. When it was possible, all non-hydrogen atoms were refined anisotropically. The H atoms were usually located in a difference map except some on solvate molecules, but those attached to carbon atoms were systematically repositioned geometrically. The H atoms were initially refined with soft restraints on the bond lengths and angles to regularize their geometry and Uiso (H) (in the range 1.2-1.5 times Ueq of the parent atom), after which the positions were refined with riding constraints. For **7**, a crystallographic disorder was found on the macrocyclic ligand of one Mn^{II} unit. For **6** and **8**, it was not possible to resolve diffuse electron-density residuals (enclosed solvent molecules). Some solvent molecules were squeezed with the SQUEEZE facility from PLATON^[60]: 5H₂O·2.5MeOH for **6** ([{Cr(L^{N3O2Ph})(CN)₂}₂Mn(H₂L^{N3O2cyclohex})]) (per asymmetric unit) and 7H₂O·2EtOH for **8** ([{Cr(L^{N3O2Ph})(CN)₂}₂Fe(H₂L^{N3O2cyclohex})]) (per asymmetric unit). Crystallographic information for all the complexes are gathered in Table 3; the CIF files are also available from The Cambridge Crystallographic Data Centre (www.ccdc.cam.ac.uk/data_request/cif) under the references CCDC-2061928 to 20611932. ORTEP plots and selected bond distances and angles are given in the supporting information.

Table 3. Selected crystallographic data and refinement parameters of **5-9**

	5	6	7	8	9
Formula ^a	C ₆₆ H ₇₃ Cr ₂ MnN ₂₁ O ₁₁	C ₇₃ H ₇₁ Cr ₂ MnN ₁₉ O ₆	C ₇₅ H ₈₉ Cr ₂ MnN ₁₉ O 21	C ₇₃ H ₇₁ Cr ₂ FeN ₁₉ O ₆	C ₇₅ H ₉₅ Cr ₂ FeN ₁₉ O ₂₄
Mw (g mol ⁻¹)	1495.36	1469.41	1751.57	1470.33	1806.53
Crystal system	monoclinic	triclinic	monoclinic	triclinic	monoclinic
Space group	<i>P2₁/c</i>	<i>P-1</i>	<i>C2</i>	<i>P-1</i>	<i>C2</i>
<i>T</i> (K)	100	100	100	100	120
<i>a</i> (Å)	17.713(1)	11.1619(3)	36.442(3)	11.188(5)	36.492(5)
<i>b</i> (Å)	23.189(2)	18.0304(6)	10.499(7)	17.970(8)	10.563(3)
<i>c</i> (Å)	18.039(1)	21.748(7)	26.932(2)	21.613(10)	26.753(4)
α (°)		72.506(1)		72.631(2)	
β (°)	93.245(2)	89.918(1)	121.240(2)	89.525(2)	121.156(3)
γ (°)		80.134(1)		80.096(2)	
<i>V</i> (Å ³)	7397.9(9)	4107.0(2)	8811.0(10)	4081.2(3)	8825.3(2)
<i>Z</i>	4	2	4	2	4
$\rho_{\text{calcd.}}$ (g cm ⁻³)	1.338	1.188	1.299	1.196	1.36
μ (mm ⁻¹)	0.527 (Mo K α)	0.469 (Mo K α)	0.460 (Mo K α)	0.495 (Mo K α)	0.486 (Mo K α)
Collected reflns	149646	84056	128393	163262	117660
Unique reflns	14568	16774	26591	15554	21867
<i>R</i> _{int}	0.065	0.056	0.058	0.06	0.080
Nb of parameters	890	910	1046	910	1116
Nb of reflns (<i>I</i> ≥ <i>n</i> σ)	11047, <i>n</i> =3	13022, <i>n</i> =3	21857, <i>n</i> =2	13018, <i>n</i> =3	15271, <i>n</i> =2
Refinement on	F	F	F ²	F	F ²
Final <i>R</i> ₁ , <i>wR</i> ₂ (<i>I</i> ≥ <i>n</i> σ) ^{b,c}	0.0537, 0.0607	0.0414, 0.0481	0.0740, 0.1923	0.0358, 0.0373	0.0654, 0.1632
Flack parameter	/	/	0.045(5)	/	0.064(19)
$\Delta\rho_{\text{min}}/\Delta\rho_{\text{max}}$	-0.99/1.59	-0.56/0.71	-0.83, 1.48	-0.50/0.79	-0.68/0.91
GOF	1.0434	1.0442	0.9524	0.9986	0.9994
CCDC n°	2061929	2061930	2061931	2061928	2061932

^a Including co-crystallized solvent molecules (except for **6** and **8** for which some solvent molecules were squeezed), ^b $R_1 = \sum ||F_o| - |F_c|| / \sum |F_o|$; ^c $wR_2 = [\sum (w(F_o^2 - F_c^2)^2) / \sum (w(F_o^2)^2)]^{1/2}$ where $w = 1/(\sigma^2(F_o^2) + (aP)^2 + bP)$ with $P = (2F_c^2 + \max(F_o^2, 0))/3$.

SUPPORTING MATERIAL

Crystallographic and geometric information; polyhedral shape analyses of the coordination spheres; additional magnetic data. The crystallographic information for the structures has been deposited at CCDC. Deposition Number(s) [CCDC-2061929](https://www.ccdc.cam.ac.uk/services/structures?id=doi:10.1002/chem.202102571) (for **5**), [CCDC-2061930](https://www.ccdc.cam.ac.uk/services/structures?id=doi:10.1002/chem.202102571) (for **6**), [CCDC-2061931](https://www.ccdc.cam.ac.uk/services/structures?id=doi:10.1002/chem.202102571) (for **7**), [CCDC-2061928](https://www.ccdc.cam.ac.uk/services/structures?id=doi:10.1002/chem.202102571) (for **8**) and [CCDC-2061932](https://www.ccdc.cam.ac.uk/services/structures?id=doi:10.1002/chem.202102571) (for **9**) contain(s) the supplementary crystallographic data for this paper. These data are provided free of charge by the joint Cambridge Crystallographic Data Centre and Fachinformationszentrum Karlsruhe <http://www.ccdc.cam.ac.uk/structures> Access Structures service.

ACKNOWLEDGEMENTS

This work was supported by the French National Research Agency, ANR, (grant ANR-17-CE07-0007). Authors are grateful to M. J.-F. Meunier (LCC) for technical assistance in magnetic, and Mössbauer data collections.

REFERENCES.

- [1] Y. Pei, O. Kahn and J. Sletten, *J. Am. Chem. Soc.* **1986**, *108*, 3143-3145.
- [2] Y. Pei, M. Verdaguer, O. Kahn, J. Sletten and J. P. Renard, *J. Am. Chem. Soc.* **1986**, *108*, 7428-7430.
- [3] H. O. Stumpf, L. Ouahab, Y. Pei, D. Grandjean and O. Kahn, *Science* **1993**, 261.
- [4] O. Kahn, *Acc. Chem. Res.* **2000**, *33*, 647-657.
- [5] C. Milios and R. P. Winpenny in *Cluster-Based Single-Molecule Magnets, Vol. 164* (Ed. S. Gao), Springer Berlin Heidelberg, **2015**, pp. 1-109.
- [6] S. Dhers, H. L. C. Feltham and S. Brooker, *Coord. Chem. Rev.* **2015**, *296*, 24-44.
- [7] M.-C. Dul, E. Pardo, R. Lescouëzec, Y. Journaux, J. Ferrando-Soria, R. Ruiz-García, J. Cano, M. Julve, F. Lloret, D. Cangussu, C. L. M. Pereira, H. O. Stumpf, J. Pasán and C. Ruiz-Pérez, *Coord. Chem. Rev.* **2010**, *254*, 2281-2296.
- [8] J. Ferrando-Soria, J. Vallejo, M. Castellano, J. Martínez-Lillo, E. Pardo, J. Cano, I. Castro, F. Lloret, R. Ruiz-García and M. Julve, *Coord. Chem. Rev.* **2017**, *339*, 17-103.
- [9] M. Verdaguer, A. Bleuzen, V. Marvaud, J. Vaissermann, M. Seuleiman, C. Desplanches, A. Sculler, C. Train, R. Garde, G. Gelly, C. Lomenech, I. Rosenman, P. Veillet, C. Cartier and F. Villain, *Coord. Chem. Rev.* **1999**, *190-192*, 1023-1047.
- [10] K. S. Pedersen, J. Bendix and R. Clerac, *Chem. Comm.* **2014**, *50*, 4396-4415.
- [11] S. Gómez-Coca, D. Aravena, R. Morales and E. Ruiz, *Coord. Chem. Rev.* **2015**, *289-290*, 379-392.
- [12] A. K. Bar, C. Pichon and J.-P. Sutter, *Coord. Chem. Rev.* **2016**, *308*, Part 2, 346-380.
- [13] C. Coulon, V. Pianet, M. Urdampilleta and R. Clérac in *Single-Chain Magnets and Related Systems, Vol. 164* (Ed. S. Gao), Springer Berlin Heidelberg, **2015**, pp. 143-184.
- [14] D. Gatteschi, R. Sessoli and J. Villain, *Molecular Nanomagnets*, Oxford University Press, Oxford, **2006**, p.
- [15] L. J. Batchelor, M. Sangalli, R. Guillot, N. Guihéry, R. Maurice, F. Tuna and T. Mallah, *Inorg. Chem.* **2011**, *50*, 12045.
- [16] T. S. Venkatakrisnan, S. Sahoo, N. Bréfuel, C. Duhayon, C. Paulsen, A.-L. Barra, S. Ramasesha and J.-P. Sutter, *J. Am. Chem. Soc.* **2010**, *132*, 6047-6056.
- [17] N. Gogoi, M. Thlijeni, C. Duhayon and J.-P. Sutter, *Inorg. Chem.* **2013**, *52*, 2283-2285.
- [18] R. Ruamps, L. J. Batchelor, R. Maurice, N. Gogoi, P. Jiménez-Lozano, N. Guihéry, C. de Graaf, A.-L. Barra, J.-P. Sutter and T. Mallah, *Chem.Eur. J.* **2013**, *19*, 950-956.
- [19] X.-C. Huang, C. Zhou, D. Shao and X.-Y. Wang, *Inorg. Chem.* **2014**, *53*, 12671-12673.
- [20] A. K. Bar, C. Pichon, N. Gogoi, C. Duhayon, S. Ramasesha and J.-P. Sutter, *Chem. Comm.* **2015**, *51*, 3616-3619.
- [21] P. Antal, B. Drahoš, R. Herchel and Z. Trávníček, *Inorg. Chem.* **2016**, *55*, 5957-5972.
- [22] M. Dey, S. Dutta, B. Sarma, R. C. Deka and N. Gogoi, *Chem. Comm.* **2016**, *52*, 753-756.
- [23] D. Shao, S.-L. Zhang, L. Shi, Y.-Q. Zhang and X.-Y. Wang, *Inorg. Chem.* **2016**, *55*, 10859-10869.
- [24] A. K. Bar, N. Gogoi, C. Pichon, V. M. L. D. P. Goli, M. Thlijeni, C. Duhayon, N. Suaud, N. Guihéry, A.-L. Barra, S. Ramasesha and J.-P. Sutter, *Chem.Eur. J.* **2017**, *23*, 4380-4396.
- [25] Y.-F. Deng, B. Yao, P.-Z. Zhan, D. Gan, Y.-Z. Zhang and K. R. Dunbar, *Dalton Trans.* **2019**, *48*, 3243-3248.
- [26] A. Mondal, S.-Q. Wu, O. Sato and S. Konar, *Chem.Eur. J.* **2020**, *26*, 4780-4789.

- [27] C. Pichon, B. Elrez, V. Béreau, C. Duhayon and J.-P. Sutter, *Eur. J. Inorg. Chem.* **2018**, 2018, 340-348.
- [28] D.-Q. Wu, D. Shao, X.-Q. Wei, F.-X. Shen, L. Shi, D. Kempe, Y.-Z. Zhang, K. R. Dunbar and X.-Y. Wang, *J. Am. Chem. Soc.* **2017**, 139, 11714-11717.
- [29] S. Chorazy, A. M. Majcher, M. Koziel, J. Kobylarczyk, S.-i. Ohkoshi and R. Podgajny, *Chem. Eur. J.* **2018**, 24, 15533-15542.
- [30] D. K. Kempe, B. S. Dolinar, K. R. Vignesh, T. J. Woods, M. R. Saber and K. R. Dunbar, *Chem. Comm.* **2019**, 55, 2098-2101.
- [31] J. Yang, Y.-F. Deng, X.-Y. Zhang, X.-Y. Chang, Z.-P. Zheng and Y.-Z. Zhang, *Inorg. Chem.* **2019**, 58, 7127-7130.
- [32] Y. Liu, Y.-C. Chen, J. Liu, W.-B. Chen, G.-Z. Huang, S.-G. Wu, J. Wang, J.-L. Liu and M.-L. Tong, *Inorg. Chem.* **2020**, 59, 687-694.
- [33] C. Pichon, N. Suaud, C. Duhayon, N. Guihéry and J.-P. Sutter, *J. Am. Chem. Soc.* **2018**, 140, 7698-7704.
- [34] K. Bretosh, V. Béreau, C. Duhayon, C. Pichon and J.-P. Sutter, *Inorg. Chem. Front.* **2020**, 7, 1503-1511.
- [35] A. Rodríguez-Forteza, P. Alemany, S. Alvarez, E. Ruiz, A. Sculler, C. Decroix, V. Marvaud, J. Vaissermann, M. Verdaguer, I. Rosenman and M. Julve, *Inorg. Chem.* **2001**, 40, 5868-5877.
- [36] D. Casanova, P. Alemany, J. M. Bofill and S. Alvarez, *Chem.—Eur. J.* **2003**, 9, 1281-1295.
- [37] S. Alvarez, P. Alemany, D. Casanova, J. Cirera, M. Llunell and D. Avnir, *Coord. Chem. Rev.* **2005**, 249, 1693-1708.
- [38] M. C. Llunell, D.; Cirera, J.; Alemany, P.; Alvarez, S., *Shape program, version 2; Universitat de Barcelona: Barcelona, Spain* **2010**.
- [39] N. F. Chilton, R. P. Anderson, L. D. Turner, A. Soncini and K. S. Murray, *J. Comput. Chem.* **2013**, 34, 1164-1175.
- [40] C. Dekker, A. F. M. Arts, H. W. de Wijn, A. J. van Duynveldt and J. A. Mydosh, *Phys. Rev. B* **1989**, 40, 11243-11251.
- [41] C. Angeli, R. Cimiraglia and J.-P. Malrieu, *Chem. Phys. Lett.* **2001**, 350, 297-305.
- [42] C. Angeli, R. Cimiraglia, S. Evangelisti, T. Leininger and J.-P. Malrieu, *J. Chem. Phys.* **2001**, 114, 10252-10264.
- [43] C. Angeli, R. Cimiraglia and J.-P. Malrieu, *J. Chem. Phys.* **2002**, 117, 9138-9153.
- [44] C. Bloch, *Nuclear Physics* **1958**, 6, 329-347.
- [45] J. des Cloizeaux, *Nuclear Physics* **1960**, 20, 321-346.
- [46] P.-Å. Malmqvist and B. O. Roos, *Chem. Phys. Lett.* **1989**, 155, 189-194.
- [47] M. Atanasov, D. Ganyushin, K. Sivalingam and F. Neese in *A Modern First-Principles View on Ligand Field Theory Through the Eyes of Correlated Multireference Wavefunctions, Vol. 143* Eds.: D. M. P. Mingos, P. Day and J. P. Dahl), Springer Berlin Heidelberg, Berlin, Heidelberg, **2012**, pp. 149-220.
- [48] Ł. Popiołek, J. Stefańska, M. Kiełczykowska, I. Musik, A. Biernasiuk, A. Malm and M. Wujec, *J. Heter. Chem.* **2016**, 53, 393-402.
- [49] G. J. Palenik and D. W. Wester, *Inorg. Chem.* **1978**, 17, 864-870.
- [50] G. Li, L. Wang, Q. Han and W. Liu, *Dalton Trans.* **2019**, 48, 14595-14599.
- [51] P. Kaur, Jyoti, W. T. Robinson and K. Singh, *J. Coord. Chem.* **2002**, 55, 281-285.
- [52] A. Bonardi, S. Ianelli, C. Pelizzi, G. Pelizzi and C. Solinas, *Inorg. Chim. Acta* **1995**, 232, 211-216.
- [53] O. Kahn, *Molecular Magnetism*, VCH, Weinheim, **1993**, p.
- [54] J. P. Perdew, K. Burke and M. Ernzerhof, *Phys. Rev. Lett.* **1996**, 77, 3865-3868.
- [55] F. Weigend and R. Ahlrichs, *Phys. Chem. Chem. Phys.* **2005**, 7, 3297-3305.

- [56] U. Ekström, L. Visscher, R. Bast, A. J. Thorvaldsen and K. Ruud, *J. Chem. Theo. Comp.* **2010**, *6*, 1971-1980.
- [57] F. Neese, *Comp. Mol. Sci.* **2012**, *2*, 73-78.
- [58] P. W. Betteridge, J. R. Carruthers, R. I. Cooper, K. Prout and D. J. Watkin, *J. Appl. Cryst.* **2003**, *36*, 1487.
- [59] W. Schmitz, *Kristall und Technik* **1975**, *10*, K120-K120.
- [60] P. van der Sluis and A. L. Spek, *Acta Cryst.* **1990**, *A46*, 194-201.

TABLE OF CONTENT.

Experimental: NMR spectra of $\text{H}_2\text{L}^{\text{N}3\text{O}2\text{cyclohex}}$

Table SI1. Continuous Shape Measures calculations.

Figure SI1. Structural comparison of the trinuclear $[\text{Cr}_2\text{Fe}]$ units.

Figure SI2. Molecular structure views for $[\{\text{Cr}(\text{L}^{\text{N}3\text{O}2\text{Ph}})(\text{CN})_2\}_2\text{Mn}(\text{H}_2\text{L}^{\text{N}3\text{O}2\text{NH}_2})] \cdot 5\text{MeOH}$, **5**

Table SI2. Selected bond lengths for **5**.

Table SI3. Selected bond angles for **5**.

Figure SI3. Comparison of the experimental and calculated powder X-ray diffractogram of **5**.

Figure SI4. Molecular structure for $[\{\text{Cr}(\text{L}^{\text{N}3\text{O}2\text{Ph}})(\text{CN})_2\}_2\text{Mn}(\text{H}_2\text{L}^{\text{N}3\text{O}2\text{cyclohex}})] \cdot 5\text{H}_2\text{O} \cdot 2.5\text{MeOH}$, **6**.

Table SI4. Selected bond lengths for **6**.

Table SI5. Selected bond angles for **6**.

Figure SI5. Comparison of the experimental and calculated powder X-ray diffractogram of **6**.

Figure SI6. Molecular structure views for $[\{\text{Cr}(\text{L}^{\text{N}3\text{O}2\text{Ph}})(\text{CN})_2\}_2\text{Mn}(\text{H}_2\text{L}^{\text{N}3\text{O}2\text{S-mand}})] \cdot 13\text{H}_2\text{O}$, **7**.

Table SI6. Selected bond lengths for **7**.

Table SI7. Selected bond angles for **7**.

Figure SI7. Comparison of the experimental and calculated powder X-ray diffractogram of **7**.

Figure SI8. Molecular structure views for $[\{\text{Cr}(\text{L}^{\text{N}3\text{O}2\text{Ph}})(\text{CN})_2\}_2\text{Fe}(\text{H}_2\text{L}^{\text{N}3\text{O}2\text{cyclohex}})] \cdot 7\text{H}_2\text{O} \cdot 2\text{MeOH}$, **8**.

Table SI8. Selected bond lengths for **8**.

Table SI9. Selected bond angles for **8**.

Figure SI9. Comparison of the experimental and calculated powder X-ray diffractogram of **8**.

Figure SI10. ^{57}Fe Mossbauer of **8**.

Figure SI11. Molecular structure views for $[\{\text{Cr}(\text{L}^{\text{N}3\text{O}2\text{Ph}})(\text{CN})_2\}_2\text{Fe}(\text{H}_2\text{L}^{\text{N}3\text{O}2\text{mand}})] \cdot 16\text{H}_2\text{O}$, **9**.

Table SI10. Selected bond lengths for **9**.

Table SI11. Selected bond angles for **9**.

Figure SI12. Comparison of the experimental and calculated powder X-ray diffractogram of **9**.

Figure SI13. ^{57}Fe Mossbauer of **9**.

Figure SI14. Temperature dependence of $\chi_M T$ for **5**, **6**, and **8** with the best fit.

Figure SI15. M vs. H curves measured at 2 K of **5-7**.

Figure SI16. M vs. H curves measured between 2 and 8 K of **8** and **9**.

Figure SI17. Temperature dependence of $\chi_M T$ of **5** and **9** at 1000 Oe with the best fit without intermolecular interactions.

Figure SI18. Compound **8**: Temperature dependence of the out-of-phase ac signal (χ_M'') at 2 K for different DC fields.

Figure SI19. Compound **9**: Temperature dependence of the out-of-phase ac signal (χ_M'') at 3 K for different DC fields.

Figure SI20. Compound **9**: Frequency and temperature dependence of the in-phase (χ_M') and out-of-phase (χ_M'') ac signals at 0 Oe.

Figure SI21. Compound **9**: Cole-Cole plots at 0 Oe.

Figure SI22. Compound **9**: Frequency and temperature dependence of the in-phase (χ_M') and out-of-phase (χ_M'') ac signals at 1000 Oe.

Figure SI23. Compound **9**: Cole-Cole plots at 1000 Oe.

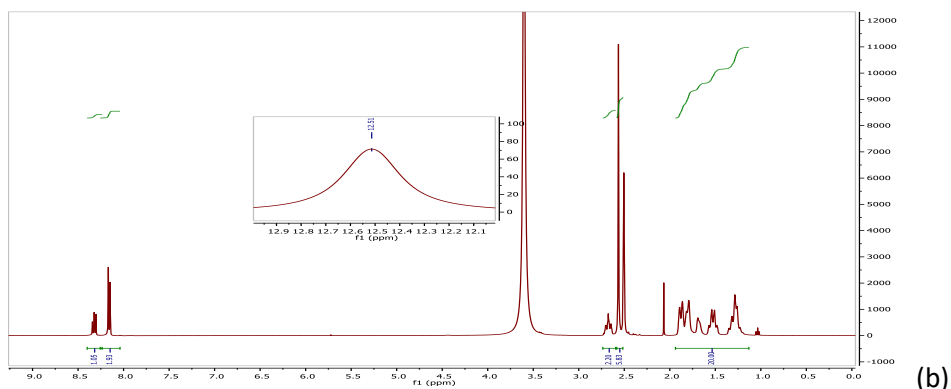
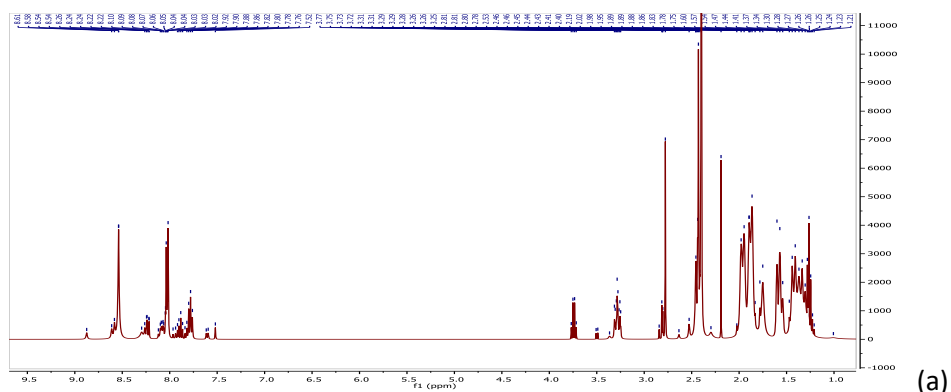
Figure SI24. Calculated (full lines) and experimental (O) $M = f(H)$ behaviors for **8** and **9**.

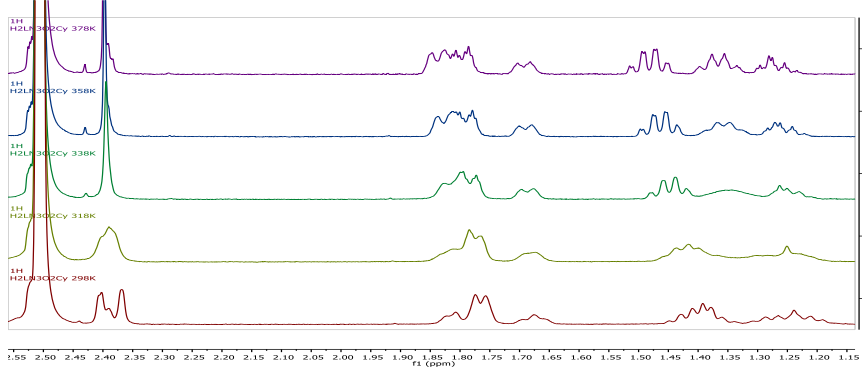
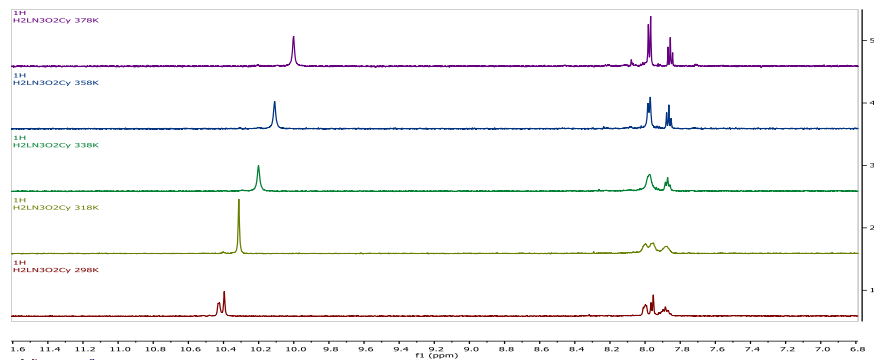
Table SI12. Coordinates of the molecular fragment used as model complex

Figure SI25: MO d_{xz} , d_{yz} , $d_{x^2-y^2}$, d_{xy} , and d_{z^2} of the symmetric model complex

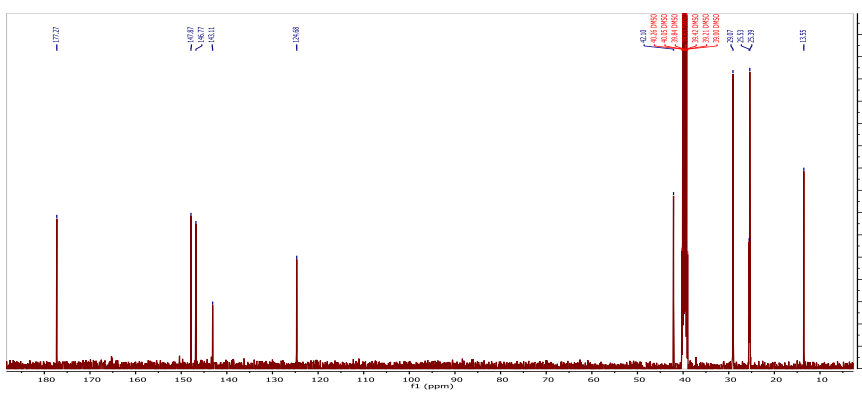
Experimental: NMR spectra of $\text{H}_2\text{L}^{\text{N3O2cyclohex}}$: (a) ^1H NMR without ZnNO_3 ; (b) ^1H NMR with ZnNO_3 ; (c) ^1H VTNMR (variable temperature NMR) and (d) ^{13}C NMR.

Interpretation of the NMR spectra (Figure SI1a) of the ligand $\text{H}_2\text{L}^{\text{N3O2cyclohex}}$ is more complex than its phenyl or amine homologous with the presence of conformers and rotamers due to the more flexible cyclohexyl moieties. The following NMR study confirms the presence of isomers. First, coordination on $\text{Zn}(\text{NO}_3)_2$ salts makes any rotation or delocalisation impossible and increase the solubility thus allowing a greatly improved spectra (Figure SI1b). Variable Temperature NMR (600MHz) between 298 K and 378 K showed the coalescence of the broad signals upon heating (Figure SI1c).





(c)



(d)

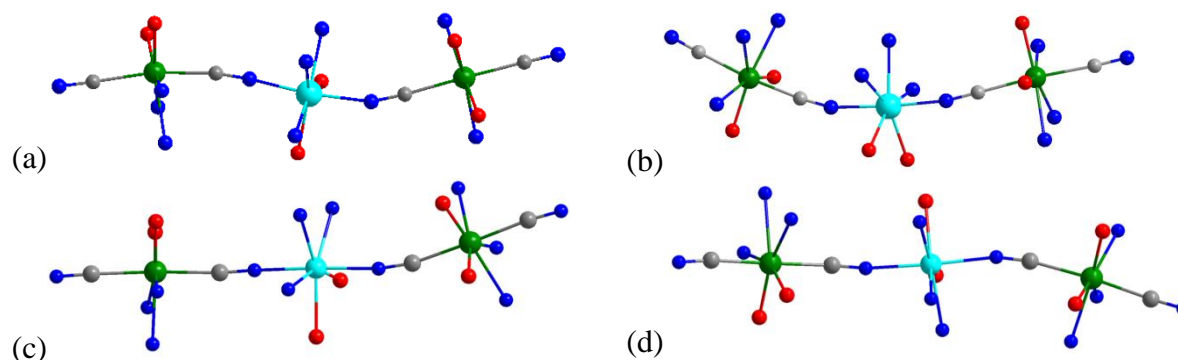
Table SII. Continuous Shape Measures calculation using SHAPE¹ with the closest geometries for each metal center highlighted in blue.

Heptacoordinated centers²

PBPY-7 D_{5h} Pentagonal bipyramid
 CTPR-7 C_{2v} Capped trigonal prism
 JPBPY-7 D_{5h} Johnson pentagonal bipyramid J13

Metal center	PBPY-7	CTPR-7	JPBPY-7
Cr1@5	0.385	6.156	3.455
Cr2@5	0.344	5.991	3.372
Mn1@5	0.718	5.355	3.515
Cr1@6	0.336	6.013	3.426
Cr2@6	0.227	6.048	3.447
Mn1@6	0.603	6.015	3.382
Cr1@7	0.502	5.455	3.804
Cr2@7	0.523	5.582	3.740
Mn1@7	0.525	5.634	3.866
Mn2A@7 ³	–	–	–
Mn2B@7 ³	–	–	–
Cr1@8	0.343	5.987	3.385
Cr2@8	0.227	6.048	3.447
Fe1@8	0.343	5.987	3.385
Cr1@9	0.493	5.420	3.776
Cr2@9	0.535	5.450	3.825
Fe1@9	0.365	5.622	3.470
Fe2@9	0.331	5.609	3.504

Figure SII. Distortions of the Cr-Fe-Cr assemblage in (a) {Cr₂FeNH₂}, (b) **8**, and (c,d) the two complexes in **9**.



¹ Llunell, M.; Casanova, D.; Cirera, J.; Alemany, P.; Alvarez, S. *SHAPE: Program for the stereochemical analysis of molecular fragments by means of continuous shape measures and associated tools*, 2.1; University of Barcelona: Barcelona, 2013.

² D. Casanova, P. Alemany, J. M. Bofill, S. Alvarez, *Chem. Eur. J.*, 2003, **9**, 1281.

³ Not analyzed because of crystallographic disorder.

Figure SI2. (a) Asymmetric unit of $[\{\text{Cr}(\text{L}^{\text{N3O2Ph}})(\text{CN})_2\}_2\text{Mn}(\text{H}_2\text{L}^{\text{N3O2NH}_2})] \cdot 5\text{MeOH}$, **5** with thermal ellipsoids fixed at 30 %. (b) View of the organization in pairs promoted by an hydrogen bond. Crystal packing of **5** (c) in the (b,c) plane highlighting the organization by pairs and (d) in the (a,b) plane highlighting the layer organization. The dashed red lines materialize the shortest intermolecular metal-metal distance (indicated in Å). Color scheme: C = grey, H = black, N = blue, O = red, Cr = green, Mn = yellow.

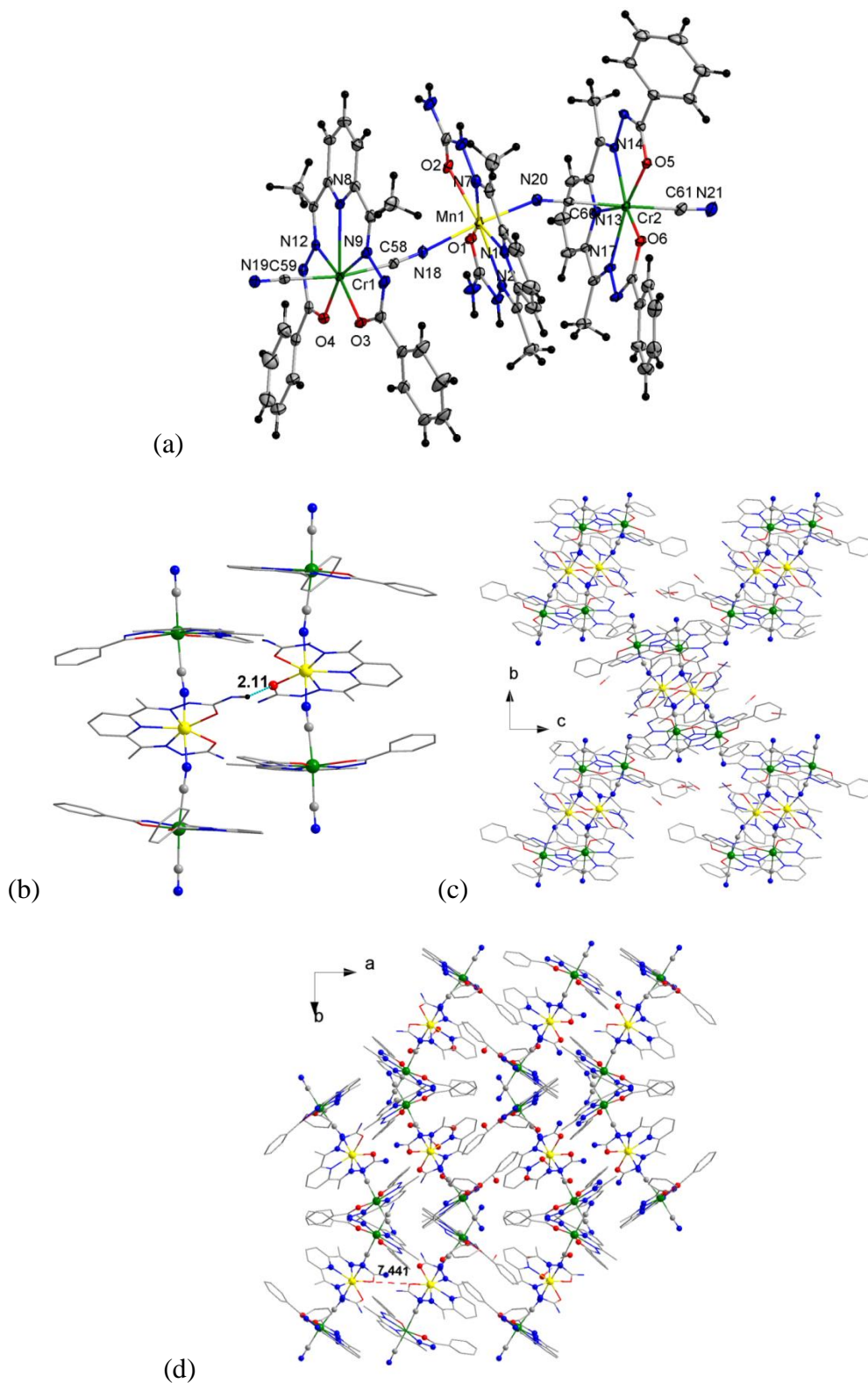


Table SI2. Selected bond lengths of **5** (Å).

Cr1–C58	2.075(3)	Cr1–C59	2.106(3)	Cr1–N8	2.457(2)
Cr1–N9	2.243(3)	Cr1–N12	2.159(2)	Cr1–O3	1.940(2)
Cr1–O4	1.998(2)	Cr2–C60	2.076(3)	Cr2–C60	2.076(3)
Cr2–C61	2.090(3)	Cr2–N13	2.392(2)	Cr2–N14	2.234(2)
Cr2–N17	2.236(2)	Cr2–O5	2.007(2)	Cr2–O6	1.943(2)
Mn1–N1	2.284(2)	Mn1–N2	2.294(2)	Mn1–N7	2.345(2)
Mn1–N18	2.176(2)	Mn1–N20	2.189(2)	Mn1–O1	2.318(2)
Mn1–O2	2.222(2)				

Table SI3. Selected bond angles of **5** (°).

C58–Cr1–C59	170.10(1)	C60–Cr2–C61	172.90(1)
C58–Cr1–N8	80.49(9)	C59–Cr1–N8	89.63(9)
C58–Cr1–N9	85.76(1)	C59–Cr1–N9	89.30(1)
N8–Cr1–N9	63.26(8)	C58–Cr1–N12	83.66(9)
C59–Cr1–N12	92.99(1)	N8–Cr1–N12	65.88(8)
N9–Cr1–N12	129.77(9)	C58–Cr1–O3	92.94(9)
C59–Cr1–O3	94.02(9)	N8–Cr1–O3	137.78(9)
N9–Cr1–O3	74.72(9)	N12–Cr1–O3	154.61(1)
C58–Cr1–O4	96.10(1)	C59–Cr1–O4	91.92(1)
N8–Cr1–O4	140.86(8)	N9–Cr1–O4	155.83(8)
N12–Cr1–O4	74.28(9)	O3–Cr1–O4	81.11(9)
C60–Cr2–N13	85.71(8)	C61–Cr2–N13	87.56(1)
C60–Cr2–N14	85.29(9)	C61–Cr2–N14	89.99(1)
N13–Cr2–N14	66.73(7)	C60–Cr2–N17	86.55(9)
C61–Cr2–N17	92.62(1)	N13–Cr2–N17	64.86(7)
N14–Cr2–N17	131.34(8)	C60–Cr2–O5	93.53(9)
C61–Cr2–O5	89.96(1)	N13–Cr2–O5	137.88(7)
N14–Cr2–O5	131.34(8)	C60–Cr2–O5	93.53(9)
C61–Cr2–O5	89.96(1)	N13–Cr2–O5	137.88(7)
N14–Cr2–O5	71.24(7)	N17–Cr2–O5	157.23(8)
C60–Cr2–O6	90.96(9)	C61–Cr2–O6	95.54(1)
N13–Cr2–O6	137.90(8)	N14–Cr2–O6	154.82(8)
N17–Cr2–O6	73.05(8)	O5–Cr2–O6	84.18(7)
N1–Mn1–N2	69.24(8)	N1–Mn1–N7	67.35(8)
N2–Mn1–N7	136.59(8)	N1–Mn1–N18	89.91(8)
N2–Mn1–N18	84.89(9)	N7–Mn1–N18	95.42(9)
N1–Mn1–N20	93.29(8)	N2–Mn1–N20	88.47(8)
N7–Mn1–N20	93.49(8)	N18–Mn1–N20	171.09(9)
N1–Mn1–O1	138.07(8)	N2–Mn1–O1	68.84(7)
N7–Mn1–O1	154.55(7)	N18–Mn1–O1	87.09(8)
N20–Mn1–O1	84.98(8)	N1–Mn1–O2	135.34(8)
N2–Mn1–O2	155.04(8)	N7–Mn1–O2	68.18(8)
N18–Mn1–O2	90.19(8)	N20–Mn1–O2	93.35(8)
O1–Mn1–O2	86.51(7)	Mn1–N18–C58	165.9(2)
Mn1–N20–C20	156.2(2)	Cr1–C58–N18	172.4(2)
Cr1–C59–N19	178.3(2)	Cr2–C60–N20	178.3(2)
Cr2–C61–N21	177.0(3)		

Figure S13. Comparison of the experimental powder X-ray diffractogram measured on polycrystalline powder introduced with their mother solution in capillary tube with the calculated ones of **5**.

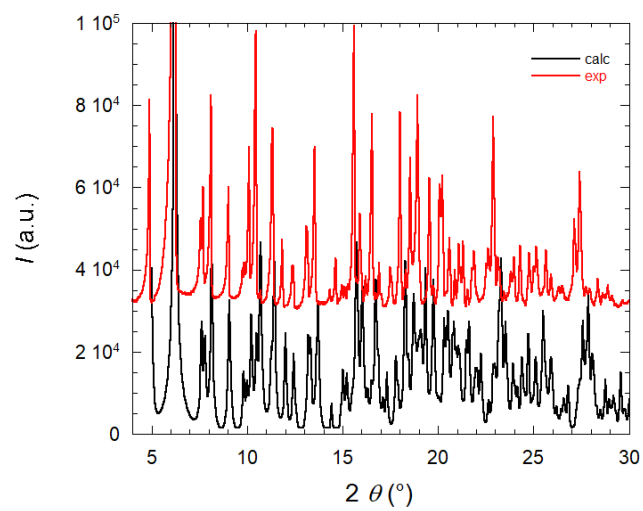


Figure S14. (a) Asymmetric unit of $[\{\text{Cr}(\text{L}^{\text{N}3\text{O}2\text{Ph}})(\text{CN})_2\}_2\text{Mn}(\text{H}_2\text{L}^{\text{N}3\text{O}2\text{cyclohex}})] \cdot 5\text{H}_2\text{O} \cdot 2.5\text{MeOH}$, **6** with thermal ellipsoids fixed at 30 %. Crystal packing of **6** (b) partial view in the (a,c) plane and (c) in the (a,c) plane highlighting the organization in layers. The dashed red lines materialize the shortest intermolecular metal-metal distance (indicated in Å). Color scheme: C = grey, H = black, N = blue, O = red, Cr = green, Mn = yellow.

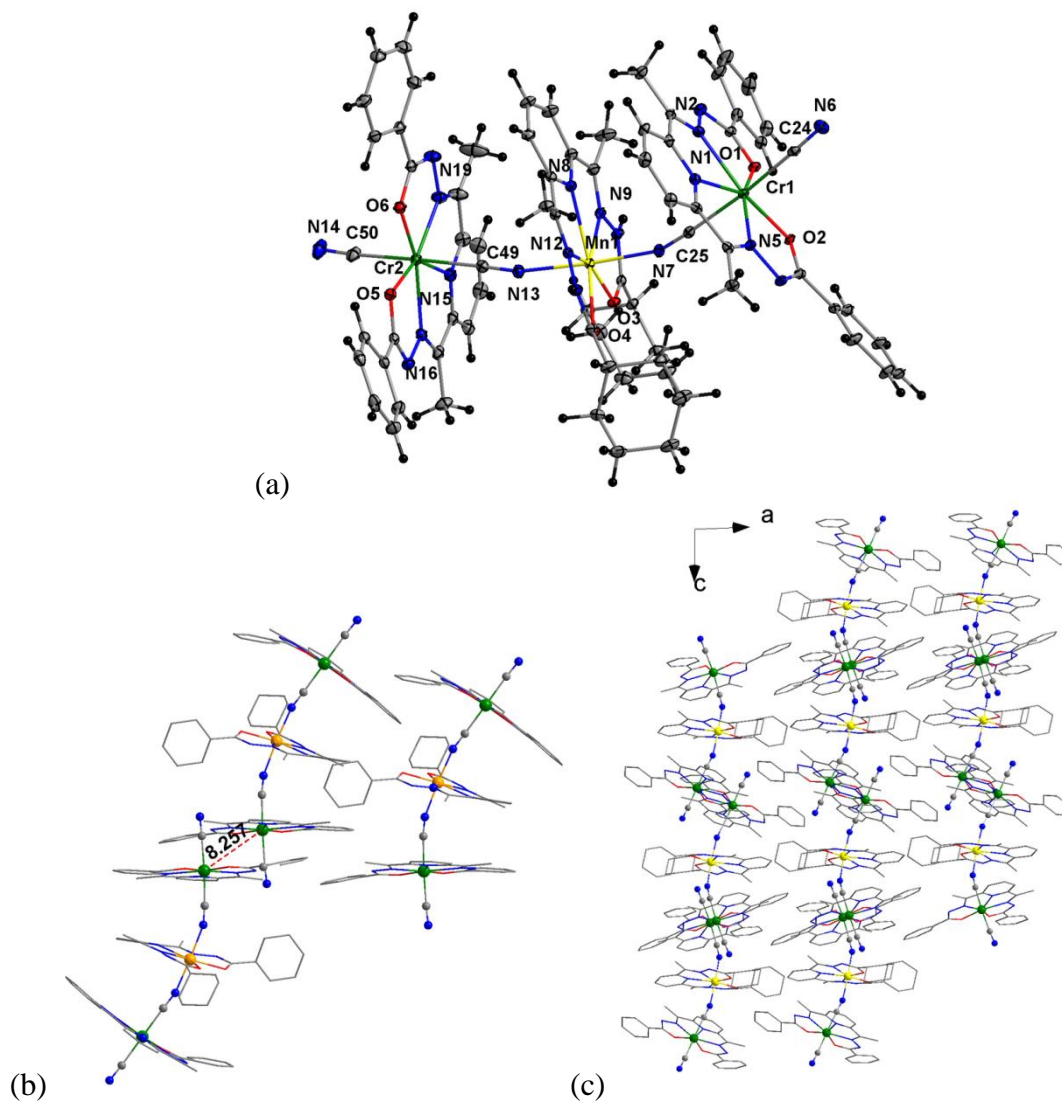


Table SI4. Selected bond lengths of **6** (Å).

Cr1–C24	2.090(2)	Cr1–C25	2.076(2)	Cr1–N1	2.415(1)
Cr1–N2	2.219 (1)	Cr1–N5	2.210(15)	Cr1–O1	1.962(1)
Cr1–O2	1.974(1)	Mn1–N7	2.187(2)	Mn1–N8	2.3530(1)
Mn1–N9	2.331(2)	Mn1–N12	2.302(2)	Mn1–N13	2.174(2)
Mn1–O3	2.252(1)	Mn1–O4	2.255(1)	Cr2–C49	2.089(2)
Cr2–C50	2.088(2)	Cr2–N15	2.375(2)	Cr2–N16	2.233(2)
Cr2–N19	2.180(2)	Cr2–O5	1.963(1)	Cr2–O6	1.954(1)

Table SI5. Selected bond angles of **6** (°).

C24–Cr1–C25	175.12(7)	C24–Cr1–N1	88.57(6)
C25–Cr1–N1	87.32(6)	C24–Cr1–N2	87.97(6)
C25–Cr1–N2	87.93(6)	N1–Cr1–N2	65.26(5)
C24–Cr1–N5	91.89(6)	C25–Cr1–N5	88.79(6)
N1–Cr1–N5	65.44(5)	N2–Cr1–N5	130.69(6)
C24–Cr1–O1	91.66(6)	C25–Cr1–O1	89.66(6)
N1–Cr1–O1	138.32(5)	N2–Cr1–O1	73.09(5)
N5–Cr1–O1	156.06(6)	C24–Cr1–O2	92.73(6)
C25–Cr1–O2	92.09(6)	N1–Cr1–O2	138.66(5)
N2–Cr1–O2	156.07(5)	N5–Cr1–O2	73.22(5)
O1–Cr1–O2	82.97(5)	N7–Mn1–N8	88.46(6)
N7–Mn1–N9	92.53(6)	N8–Mn1–N9	66.60(5)
N7–Mn1–N12	83.35(6)	N8–Mn1–N12	67.01(6)
N9–Mn1–N12	133.51(6)	N7–Mn1–N13	175.62(6)
N8–Mn1–N13	87.42(6)	N9–Mn1–N13	87.18(6)
N12–Mn1–N13	93.68(6)	N7–Mn1–O3	94.67(5)
N8–Mn1–O3	135.89(5)	N9–Mn1–O3	69.31(5)
N12–Mn1–O3	157.07(5)	N13–Mn1–O3	89.31(6)
N7–Mn1–O4	85.55(6)	N8–Mn1–O4	136.58(5)
N9–Mn1–O4	156.51(5)	N12–Mn1–O4	69.58(5)
N13–Mn1–O4	96.45(6)	O3–Mn1–O4	87.49(5)
C49–Cr2–C50	173.46(8)	C49–Cr2–N15	87.28(6)
C50–Cr2–N15	86.18(7)	C49–Cr2–N16	86.15(7)
C50–Cr2–N16	90.93(7)	N15–Cr2–N16	65.67(6)
C49–Cr2–N19	89.22(7)	C50–Cr2–N19	88.42(8)
N15–Cr2–N19	66.74(6)	N16–Cr2–N19	132.33(7)
C49–Cr2–O5	89.78(7)	C50–Cr2–O5	94.93(8)
N15–Cr2–O5	138.20(6)	N16–Cr2–O5	72.54(6)
N19–Cr2–O5	154.94(6)	C49–Cr2–O6	93.58(7)
C50–Cr2–O6	91.60(7)	N15–Cr2–O6	140.33(6)
N16–Cr2–O6	154.00(6)	N19–Cr2–O6	73.61(6)
O5–Cr2–O6	81.46(6)	Mn1–N13–C49	165.55(2)
Mn1–N7–C25	159.50(1)	Cr2–C24–N6	178.02(2)
Cr1–C25–N7	173.49(1)	Cr2–C49–N13	178.05(2)
Cr2–C50–N14	176.6(2)		

Figure S15. Comparison of the experimental powder X-ray diffractogram measured on polycrystalline powder introduced with their mother solution in capillary tube with the calculated ones of **6**.

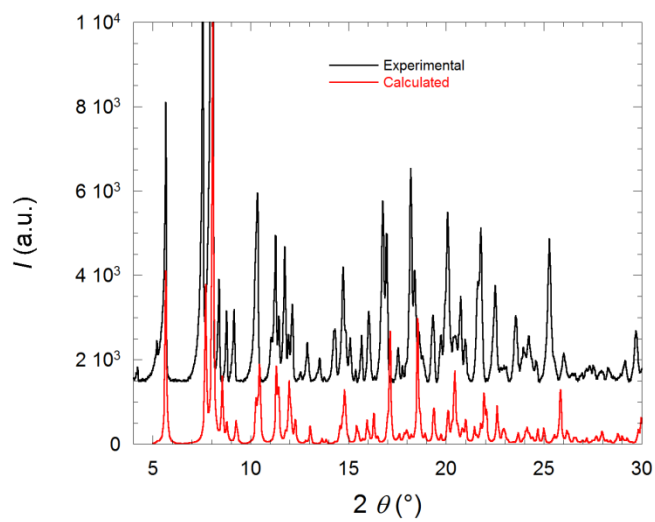


Figure SI6. (a) Molecular structure of $[\{\text{Cr}(\text{L}^{\text{N3O2Ph}})(\text{CN})_2\}_2\text{Mn}(\text{H}_2\text{L}^{\text{N3O2mand}})] \cdot 13\text{H}_2\text{O}$, **7** showing the two non-equivalent trinuclears along with the disorder on one manganese site and (b) with thermal ellipsoids fixed at 30 %. View of the crystal packing of **7** (c) in the (b,c) plane and in the (a,c) plane. The dashed red line materializes the shortest intermolecular metal-metal distance (indicated in Å). Color scheme: C = grey, H = dark grey, N = blue, O = red, K = blue green, Cr = green and Mn = yellow.

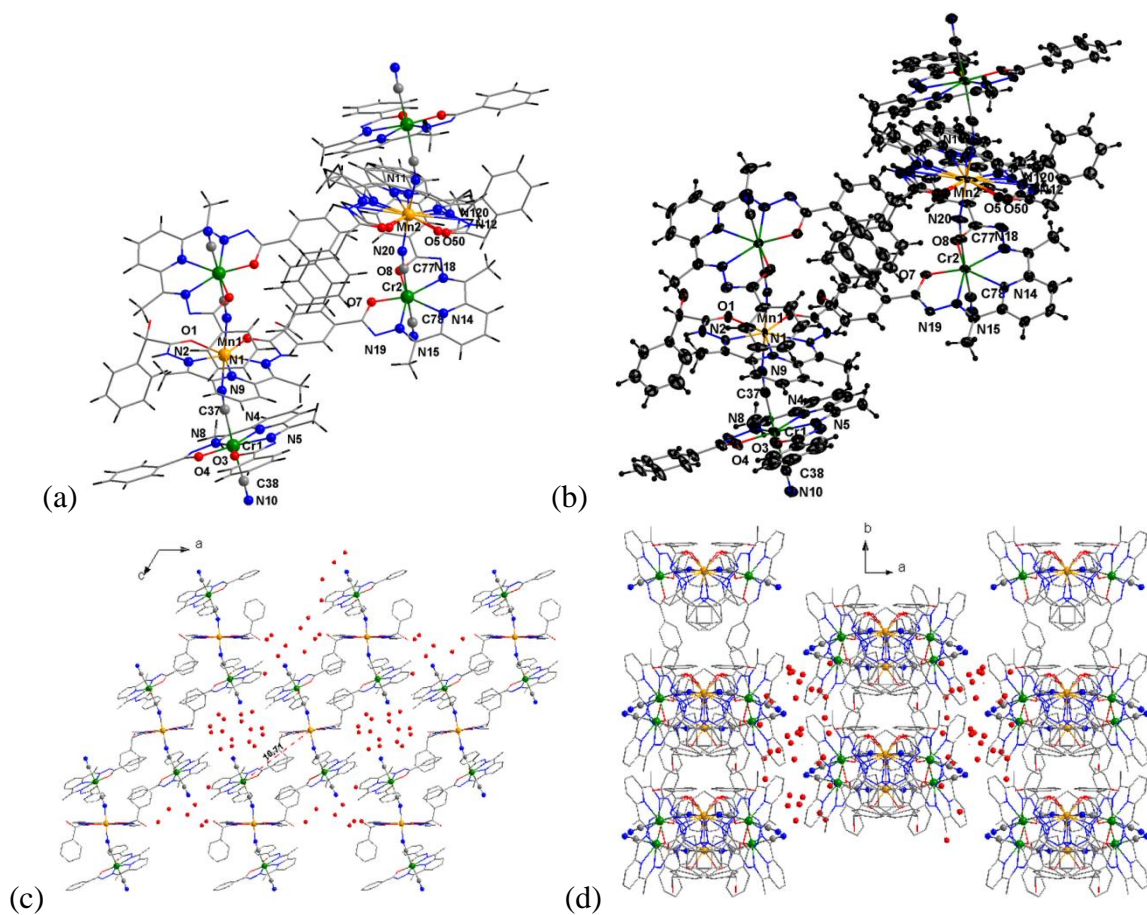


Table SI6. Selected bond lengths of **7** (Å).

Cr1–C37	2.105(4)	Cr1–C38	2.094(5)	Cr1–N4	2.392(4)
Cr1–N5	2.195(4)	Cr1–N8	2.240(4)	Cr1–O3	1.945(3)
Cr1–O4	1.963(3)	Cr2–C77	2.117(4)	Cr2–C78	2.079(4)
Cr2–N14	2.392(3)	Cr2–N15	2.204(3)	Cr2–N18	2.249(4)
Cr2–O7	1.953(3)	Cr2–O8	1.966(3)	Mn1–N9	2.251(3)
Mn1–O1	2.282(3)	Mn1–N2	2.304(3)	Mn2–N20	2.214(4)
Mn2–O50	2.095(8)	Mn2–N120	2.069(7)	Mn2–N11	2.359(7)

Table SI7. Selected bond angles of **7** (°).

C37–Cr1–C38	176.52(2)	C37–Cr1–N4	90.64(1)
C38–Cr1–N4	86.98(1)	C37–Cr1–N5	85.32(1)
C38–Cr1–N5	91.39(2)	N4–Cr1–N5	65.89(1)
C37–Cr1–N8	97.65(1)	C38–Cr1–N8	83.66(2)
N4–Cr1–N8	65.40(1)	N5–Cr1–N8	131.21(1)
C37–Cr1–O3	87.86(1)	C38–Cr1–O3	92.32(2)
N4–Cr1–O3	139.66(1)	N5–Cr1–O3	73.82(1)
N8–Cr1–O3	154.57(1)	C37–Cr1–O4	92.94(1)
C38–Cr1–O4	90.53(2)	N4–Cr1–O4	137.54(1)
N5–Cr1–O4	156.57(1)	N8–Cr1–O4	72.20(1)
O3–Cr1–O4	82.78(1)	C77–Cr2–C78	176.11(2)
C77–Cr2–N14	91.54(1)	C78–Cr2–N14	88.58(1)
C77–Cr2–N15	96.39(1)	C78–Cr2–N15	87.22(1)
N14–Cr2–N15	65.89(1)	C77–Cr2–N18	85.94(1)
C78–Cr2–N18	90.59(1)	N14–Cr2–N18	64.98(1)
N15–Cr2–N18	130.86(1)	C77–Cr2–O7	91.58(1)
C78–Cr2–O7	90.85(1)	N14–Cr2–O7	139.47(1)
N15–Cr2–O7	73.61(1)	N18–Cr2–O7	155.53(1)
C78–Cr2–O8	90.36(1)	N14–Cr2–O8	137.43(1)
N15–Cr2–O8	156.52(1)	N18–Cr2–O8	72.48(1)
O7–Cr2–O8	83.09(1)	N9–Mn1–O1	89.25(1)
N1–Mn1–N2	67.76(8)	N1–Mn1–N9	91.48(9)
N2–Mn1–N9	87.12(1)	N1–Mn1–O1	137.40(7)
N2–Mn1–O1	69.74(1)	N9–Mn1–O1	89.25(1)
N20–Mn2–O50	87.0(2)	N20–Mn2–O5	86.9(2)
N20–Mn2–N120	87.6(2)	O50–Mn2–N120	78.4(3)
O5–Mn2–N120	72.8(3)	N20–Mn2–N12	85.7(2)
O50–Mn2–N12	66.5(3)	O5–Mn2–N12	60.9(3)
N20–Mn2–N11	92.1(2)	O50–Mn2–N11	129.9(3)
O5–Mn2–N11	124.3(2)	N120–Mn2–N11	51.5(3)
N12–Mn2–N11	63.5(2)		

Figure S17. Comparison of the experimental powder X-ray diffractogram measured on polycrystalline powder introduced with their mother solution in capillary tube with the calculated ones of **7**.

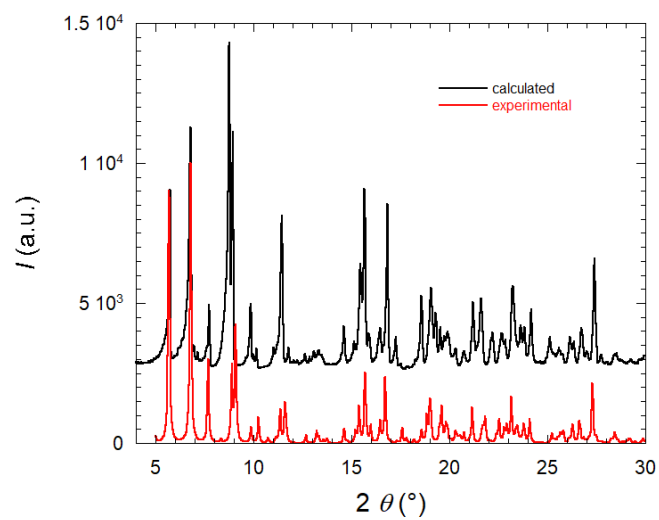


Figure S18. (a) Asymmetric unit of $[\{\text{Cr}(\text{L}^{\text{N3O2Ph}})(\text{CN})_2\}_2\text{Fe}(\text{H}_2\text{L}^{\text{N3O2cyclohex}})] \cdot 7\text{H}_2\text{O} \cdot 2\text{MeOH}$, **8** with thermal ellipsoids fixed at 30 %. Crystal packing of **8** (b) in the (b,c) plane and (c) in the (a,c) plane. The dashed red lines materialize the shortest intermolecular metal-metal distance (indicated in Å). Color scheme: C = grey, H = black, N = blue, O = red, Cr = green, Fe = cyan.

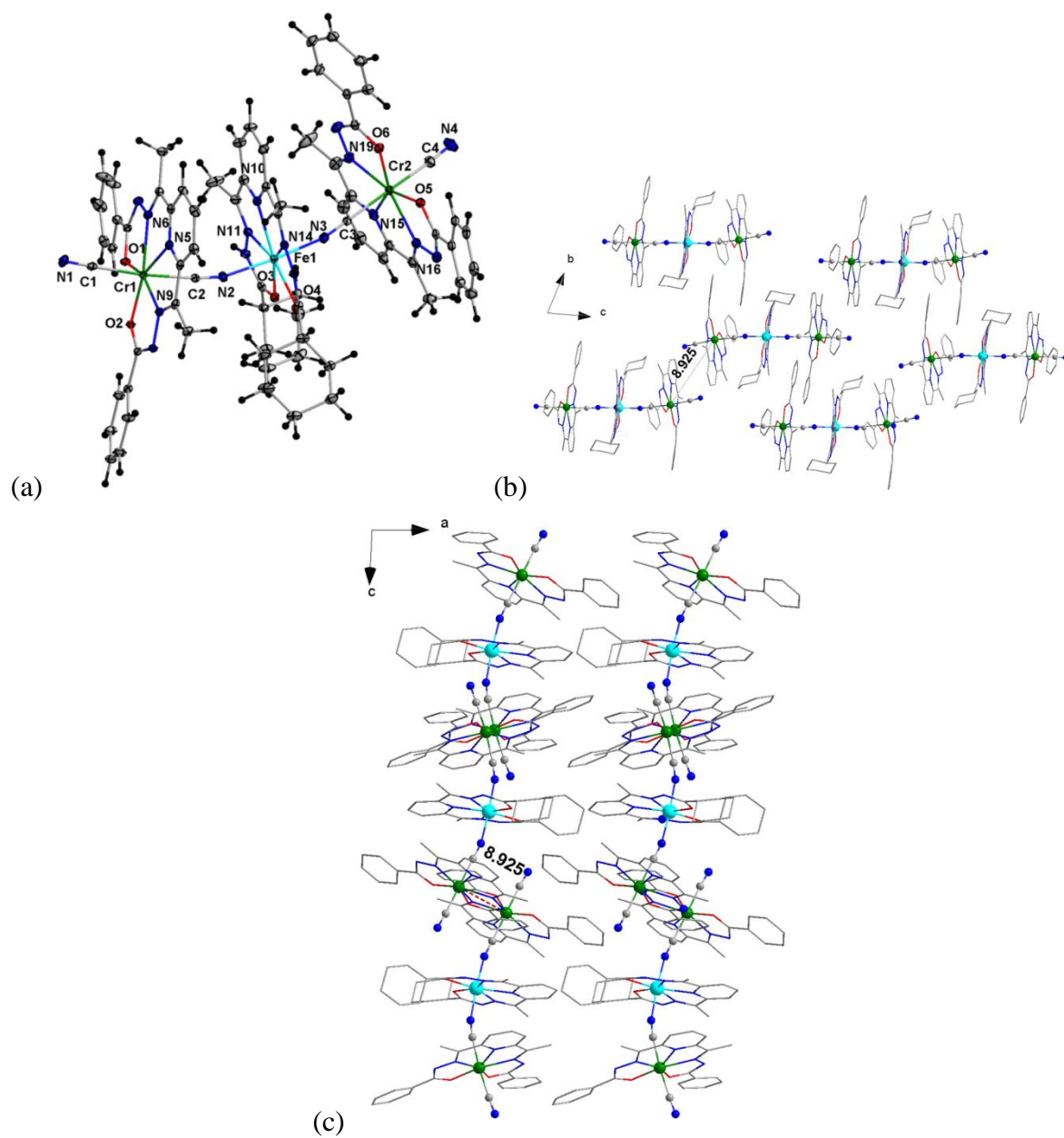


Table SI8. Selected bond lengths of **8** (Å).

Cr1–C1	2.091(2)	Cr1–C2	2.064(2)	Cr1–N5	2.413(1)
Cr1–N6	2.220(1)	Cr1–N9	2.212(2)	Cr1–O1	1.960(1)
Cr1–O2	1.974(1)	Cr2–C3	2.085(2)	Cr2–C4	2.085(1)
Cr2–N15	2.373(2)	Cr2–N16	2.231(1)	Cr2–N19	2.187(2)
Cr2–O5	1.965(1)	Cr2–O6	1.953(1)	Fe1–N2	2.117(1)
Fe1–N3	2.114(2)	Fe1–N10	2.269(1)	Fe1–N11	2.249(1)
Fe1–N14	2.230(1)	Fe1–O3	2.218(1)	Fe1–O4	2.219(13)

Table SI9. Selected bond angles of **8** (°).

C1–Cr1–C2	174.24(6)	C1–Cr1–N5	88.37(6)
C2–Cr1–N5	87.00(5)	C1–Cr1–N6	87.59(6)
C2–Cr1–N6	87.36(6)	N5–Cr1–N6	65.12(5)
C1–Cr1–N9	92.11(6)	C2–Cr1–N9	89.07(6)
N5–Cr1–N9	65.39(5)	N5–Cr1–N9	179.24(1)
N6–Cr1–N9	130.49(5)	C1–Cr1–O1	91.60(6)
C2–Cr1–O1	89.59(6)	N5–Cr1–O1	138.28(5)
N6–Cr1–O1	73.20(5)	N9–Cr1–O1	156.16(5)
O1–Cr1–O2	83.04(5)	C3–Cr2–C4	173.63(7)
C3–Cr2–N15	87.56(6)	C4–Cr2–N15	86.08(7)
C3–Cr2–N16	86.77(6)	C4–Cr2–N16	90.88(7)
N15–Cr2–N16	65.86(6)	C3–Cr2–N19	88.92(6)
C4–Cr2–N19	88.31(7)	N15–Cr2–N19	66.67(6)
N16–Cr2–N19	132.46(6)	C3–Cr2–O5	90.32(6)
C4–Cr2–O5	94.62(7)	N15–Cr2–O5	138.49(5)
N16–Cr2–O5	72.63(5)	N19–Cr2–O5	154.77(6)
C3–Cr2–O6	93.47(6)	C4–Cr2–O6	91.25(7)
N15–Cr2–O6	140.20(6)	N16–Cr2–O6	153.94(6)
N19–Cr2–O6	73.57(6)	O5–Cr2–O6	81.31(5)
N2–Fe1–N3	176.00(6)	N2–Fe1–N10	88.57(5)
N3–Fe1–N10	87.47(6)	N2–Fe1–N11	91.85(5)
N3–Fe1–N11	87.26(6)	N10–Fe1–N11	68.36(5)
N2–Fe1–N14	83.88(5)	N3–Fe1–N14	94.08(6)
N10–Fe1–N14	68.41(5)	N11–Fe1–N14	136.65(5)
N2–Fe1–O3	94.82(5)	N3–Fe1–O3	88.57(5)
N10–Fe1–O3	139.12(5)	N11–Fe1–O3	70.81(5)
N14–Fe1–O3	152.47(5)	N2–Fe1–O4	86.32(5)
N3–Fe1–O4	96.30(5)	N10–Fe1–O4	139.55(5)
N11–Fe1–O4	151.83(5)	N14–Fe1–O4	71.15(5)
O3–Fe1–O4	81.32(5)	Cr1–C1–N1	177.80(1)
Cr1–C2–N2	172.03(1)	Cr2–C3–N3	179.38(1)
Cr2–C4–N4	176.5(2)	Fe1–N2–C2	163.54(1)
Fe1–N3–C3	166.98(1)		

Figure S19 Comparison of the experimental powder X-ray diffractogram measured on polycrystalline powder introduced with their mother solution in capillary tube with the calculated one of **8**.

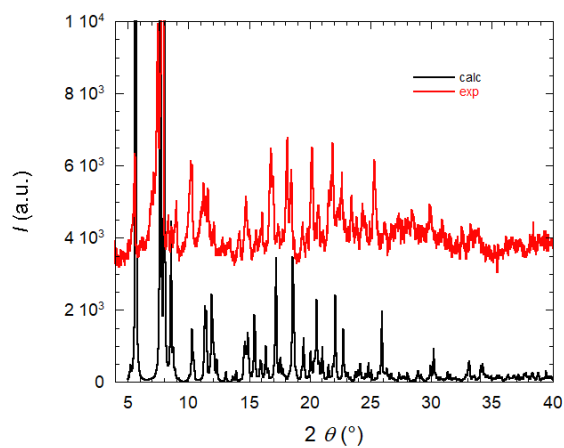


Figure S110. ⁵⁷Fe Mössbauer of **8**.

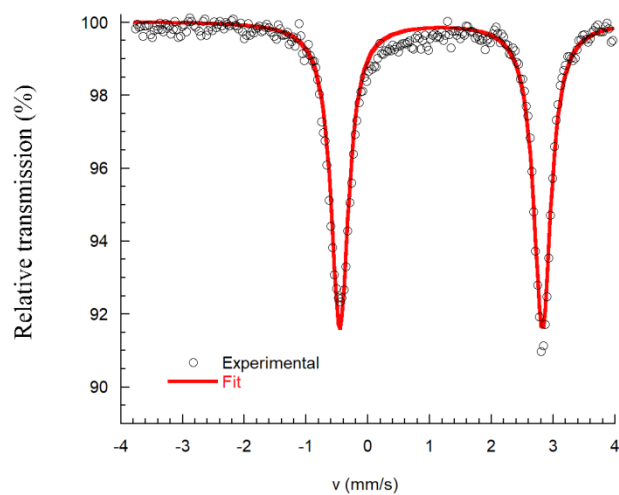


Figure SI11. (a) Asymmetric unit of $[\{\text{Cr}(\text{L}^{\text{N3O2Ph}})(\text{CN})_2\}_2\text{Fe}(\text{H}_2\text{L}^{\text{N3O2mand}})] \cdot 16\text{H}_2\text{O}$, **9** with thermal ellipsoids fixed at 30 %. Crystal packing of **9** in the (b) (*a,c*) and (c) (*b,c*) plane. The dashed red lines materialize the shortest intermolecular metal-metal distance (indicated in Å). Color scheme: C = grey, H = black, N = blue, O = red, Cr = green, Fe = cyan.

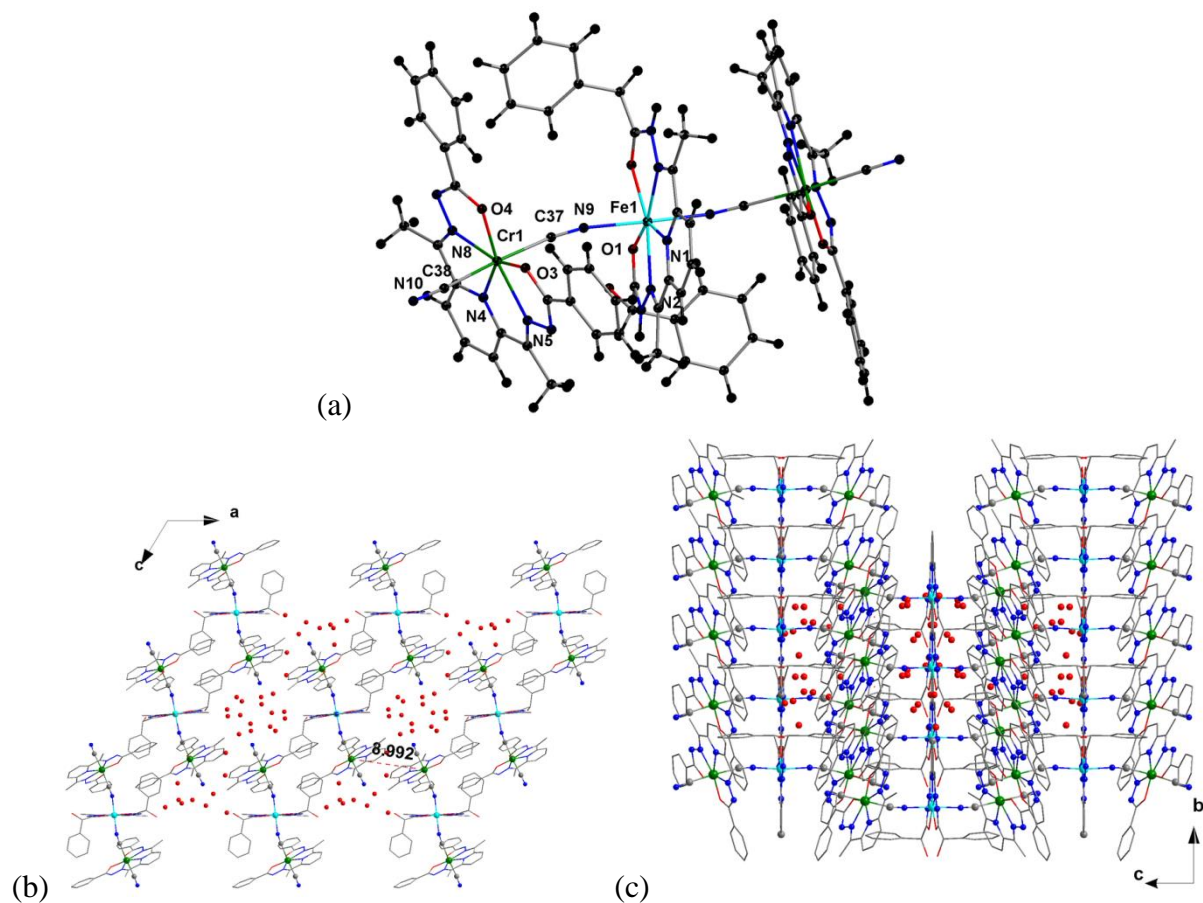


Table SI10. Selected bond lengths of **9** (Å).

Cr1–C37	2.107(5)	Cr1–C38	2.097(6)	Cr1–N4	2.377(4)
Cr1–N5	2.200(4)	Cr1–N8	2.244(5)	Cr1–O3	1.945(4)
Cr1–O4	1.969(3)	Cr2–C77	2.127(5)	Cr2–C78	2.087(6)
Cr2–N14	2.390(5)	Cr2–N15	2.203(4)	Cr2–N18	2.245(5)
Cr2–O7	1.966(3)	Cr2–O8	1.959(4)	Fe1–N9	2.172(4)
Fe1–N2	2.243(4)	Fe1–O1	2.244(4)	Fe1–N1	2.226(6)
Fe2–O5	2.211(5)	Fe2–N12	2.226(6)	Fe2–N20	2.170(4)
Fe2–N11	2.253(8)				

Table SI11. Selected bond angles of **9** (°).

C37–Cr1–C38	176.4(2)	C37–Cr1–N4	91.20(1)
C38–Cr1–N4	86.0(2)	C37–Cr1–N5	85.68(1)
C38–Cr1–N5	91.1(2)	N4–Cr1–N5	66.08(2)
C37–Cr1–N8	98.65(2)	C38–Cr1–N8	82.3(2)
N4–Cr1–N8	65.70(2)	N5–Cr1–N8	131.65(2)
C37–Cr1–O3	88.61(2)	C38–Cr1–O3	92.1(2)
N4–Cr1–O3	140.06(2)	N5–Cr1–O3	74.08(2)
C38–Cr1–O4	90.77(2)	N4–Cr1–O4	138.07(2)
N5–Cr1–O4	155.85(2)	N8–Cr1–O4	72.43(2)
C77–Cr2–N14	91.36(2)	C78–Cr2–N14	88.52(2)
C77–Cr2–N15	97.14(2)	C78–Cr2–N15	86.43(2)
N14–Cr2–N15	65.64(1)	C77–Cr2–N18	85.85(2)
C78–Cr2–N18	90.51(2)	N14–Cr2–N18	64.90(2)
N15–Cr2–18	130.50(2)	C77–Cr2–O7	92.09(2)
C78–Cr2–O7	90.57(2)	N14–Cr2–O7	139.27(2)
N15–Cr2–O7	73.66(1)	N18–Cr2–O7	155.83(2)
C77–Cr2–O8	86.90(2)	C78–Cr2–O8	90.5(2)
N14–Cr2–O8	137.55(2)	N15–Cr2–O8	156.58(2)
N18–Cr2–O8	72.68(2)	O7–Cr2–O8	83.17(2)
N1–Fe1–N2	68.89(1)	N1–Fe1–N9	91.65(2)
N2–Fe1–N9	86.20(1)	N1–Fe1–O1	139.67(9)
N2–Fe1–O1	151.20(1)	N9–Fe1–O1	88.78(1)
N20–Fe2–O5	86.97(2)	N20–Fe2–N12	86.49(2)
O5–Fe2–N12	70.3(2)	N20–Fe2–N11	92.78(1)
O5–Fe2–N11	140.16(1)	N12–Fe2–N11	69.91(2)

Figure SI12. Comparison of the experimental powder X-ray diffractogram measured on polycrystalline powder introduced with their mother solution in capillary tube with the calculated one of **9**.

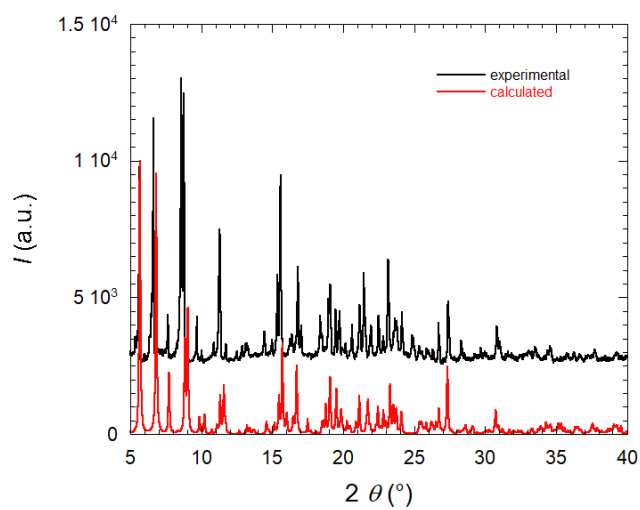


Figure SI13. ^{57}Fe Mössbauer of **9**.

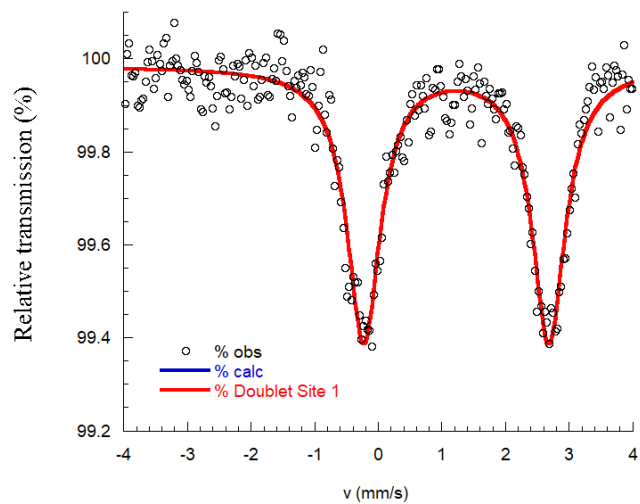


Figure SI14. Experimental (O) and calculated (—) temperature dependence of $\chi_M T$ for **5** (a), **6** and **8** (b) with best fits.

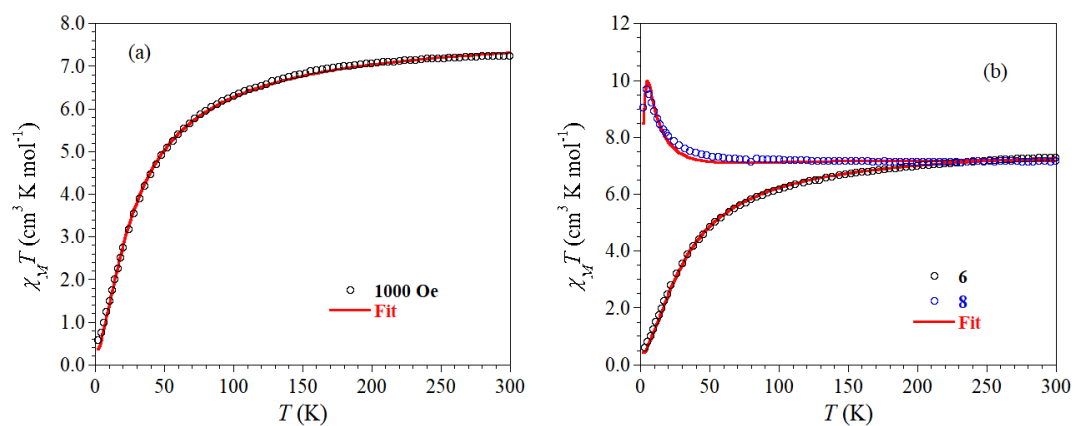


Figure SI15. M vs. H curves measured at 2 K of (left) **5-7**.

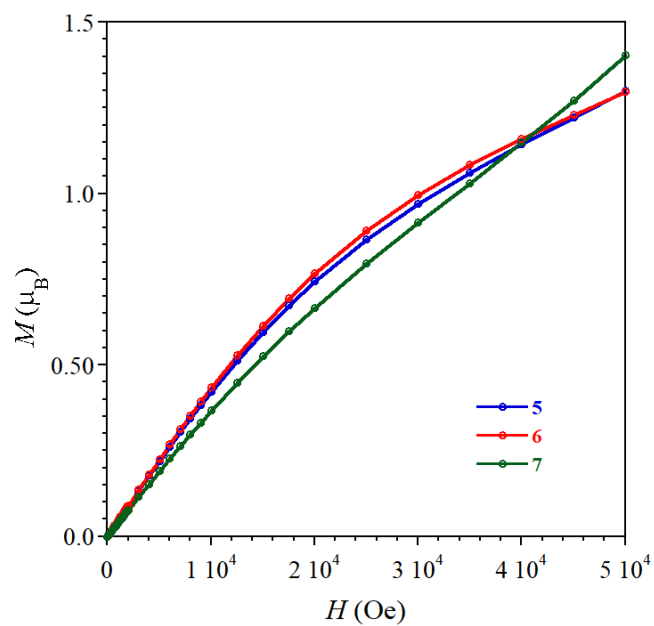


Figure SI16. Field dependence of the magnetization measured between 2 K and 8 K for (a) **8** and (b) **9**. The solid lines are guides for the eyes.

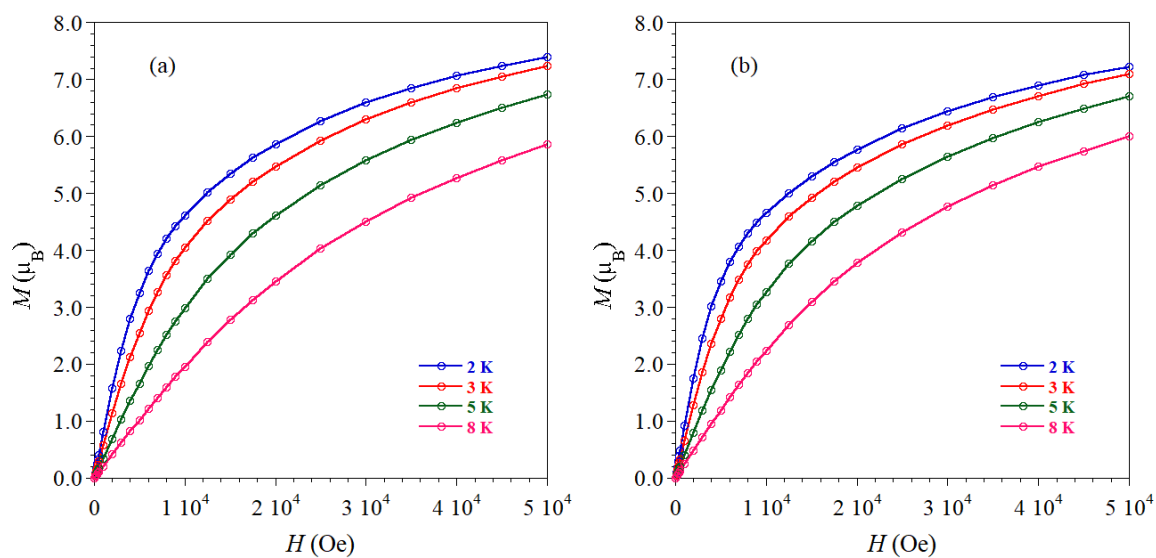
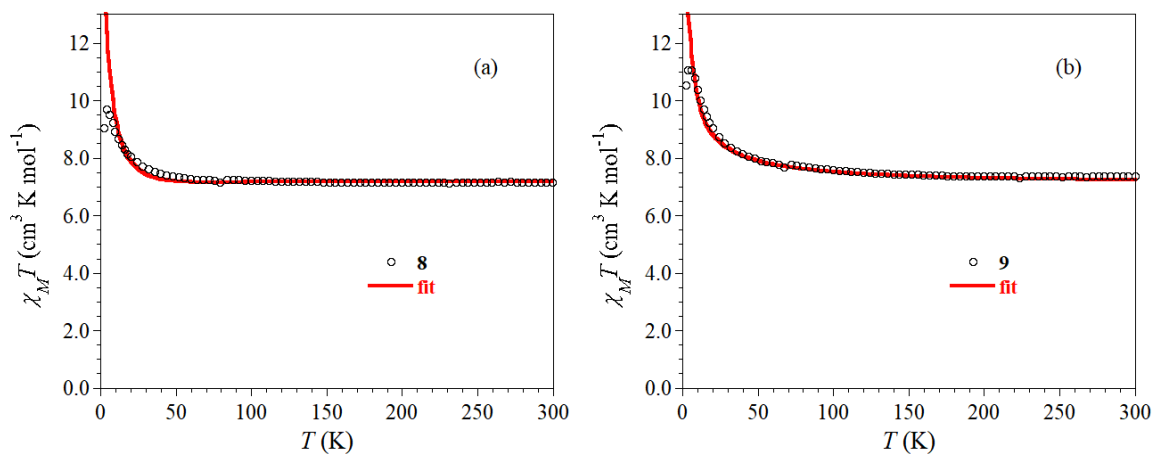


Figure SI17. Temperature dependence of $\chi_M T$ of (a) **8** and (b) **9** at 1000 Oe with the best fit without intermolecular interactions.



Best fit parameters are for **8**: $J = 2.00 \pm 0.01 \text{ cm}^{-1}$, $D_{\text{Fe}} = -17.8 \pm 0.1 \text{ cm}^{-1}$ and $g = 2.10$; for **9**: $J = 2.00 \pm 0.01 \text{ cm}^{-1}$, $D_{\text{Fe}} = -12 \pm 3 \text{ cm}^{-1}$ and $g = 2.10$.

Figure SI18. Compound **8**: Temperature dependence of the out-of-phase ac signal (χ_M'') between 2 and 6 K for different DC fields.

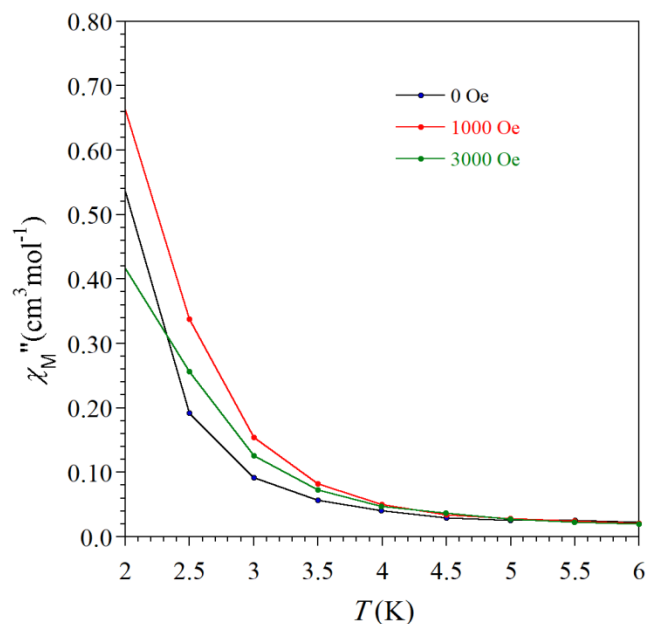


Figure SI19. Compound **9**: (a) Temperature dependence of the out-of-phase ac signal (χ_M'') at 3 K for different DC fields and (b) field dependence of the relaxation time at 3 K.

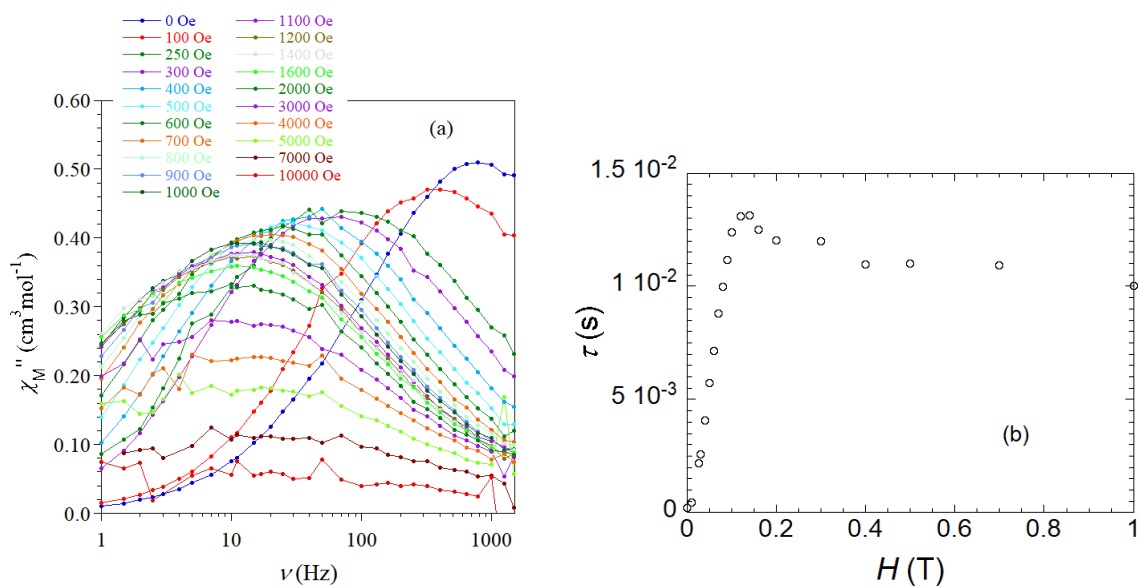


Figure SI20. Temperature and frequency dependence of the in-phase (χ') and out-of-phase (χ'') ac susceptibilities recorded at 0 Oe dc field with a 3 Oe ac field with frequencies and temperatures ranging from 1 to 1500 Hz and 2 to 8 K, respectively for **9**. Solid lines in (d) are best fits to the Debye model.

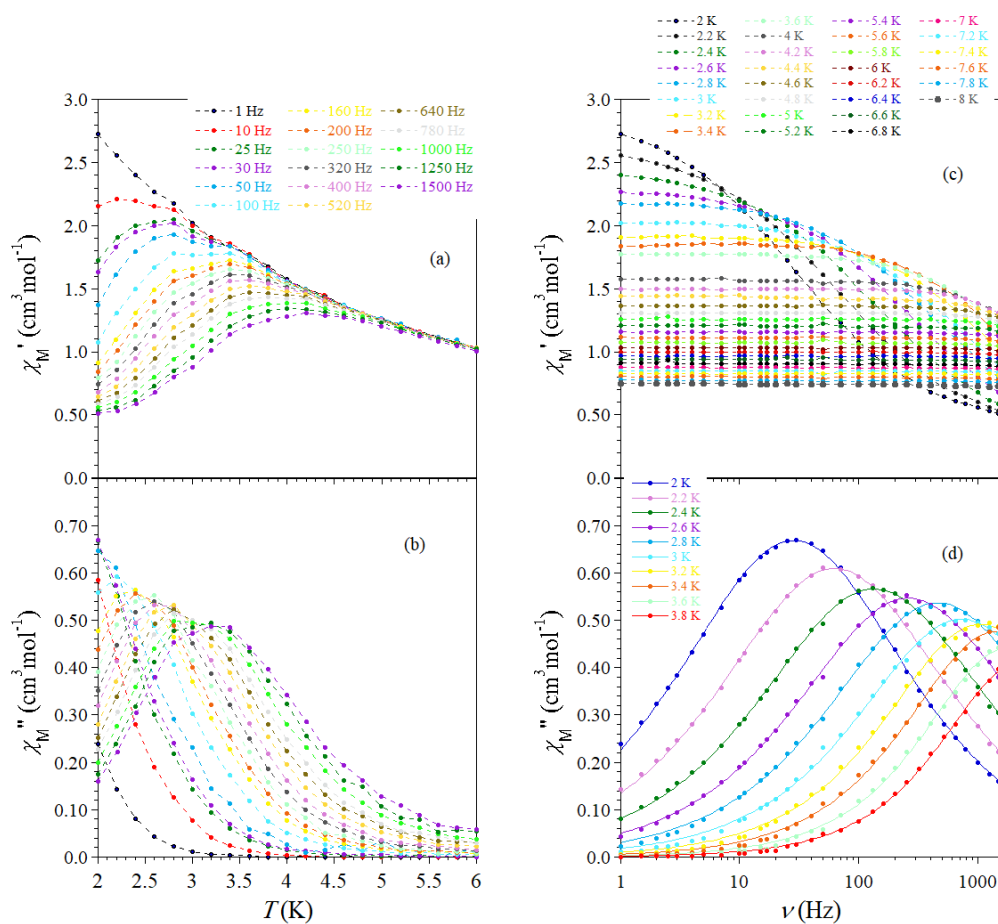
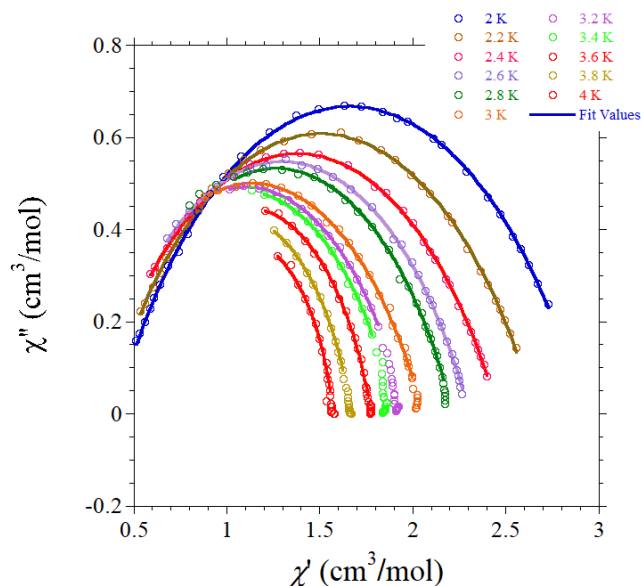


Figure SI21. Cole-Cole ($\chi'' = f(\chi')$) plots for **9** between 2 and 3.8 K at 0 Oe with the best fits to the generalized Debye model (equation 1)⁴; the best fit parameters are given in the table.



T (K)	χ_T ($\text{cm}^3 \text{mol}^{-1}$)	χ_S ($\text{cm}^3 \text{mol}^{-1}$)	α	R^2
2	2.9208	0.39337	0.38059	0.99965
2.2	2.6627	0.34683	0.38367	0.99957
2.4	2.4616	0.29175	0.38675	0.99998
2.6	2.304	0.28925	0.36529	0.99963
2.8	2.2151	0.31567	0.34825	0.99975
3	2.0526	0.22197	0.3622	0.99982
3.2	1.9595	0.25553	0.3327	0.99967
3.4	1.9007	0.28739	0.31275	0.99993
3.6	1.775	0.46702	0.23747	0.99951
3.8	1.669	0.43051	0.22791	0.99994

$$\chi'' = (\chi_T - \chi_S) \tan\left(\frac{\pi\alpha}{2}\right) + \sqrt{\left[\left(\frac{\chi_T - \chi_S}{2}\right)^2 \left\{ \left[\tan\left(\frac{\pi\alpha}{2}\right) \right]^2 + 1 \right\} - \left(\chi' - \frac{\chi_S + \chi_T}{2}\right)^2\right]} \quad \text{equation 1}$$

⁴ K. S. Cole, R. H. Cole, *J. Chem. Phys.* **1941**, 9, 341.

Figure SI22. Temperature and frequency dependence of the in-phase (χ') and out-of-phase (χ'') ac susceptibilities recorded at 1000 Oe dc field with a 3 Oe ac field with frequencies and temperatures ranging from 1 to 1500 Hz and 2 to 8 K, respectively for **9**. Solid lines in (d) are best fits to the Debye model.

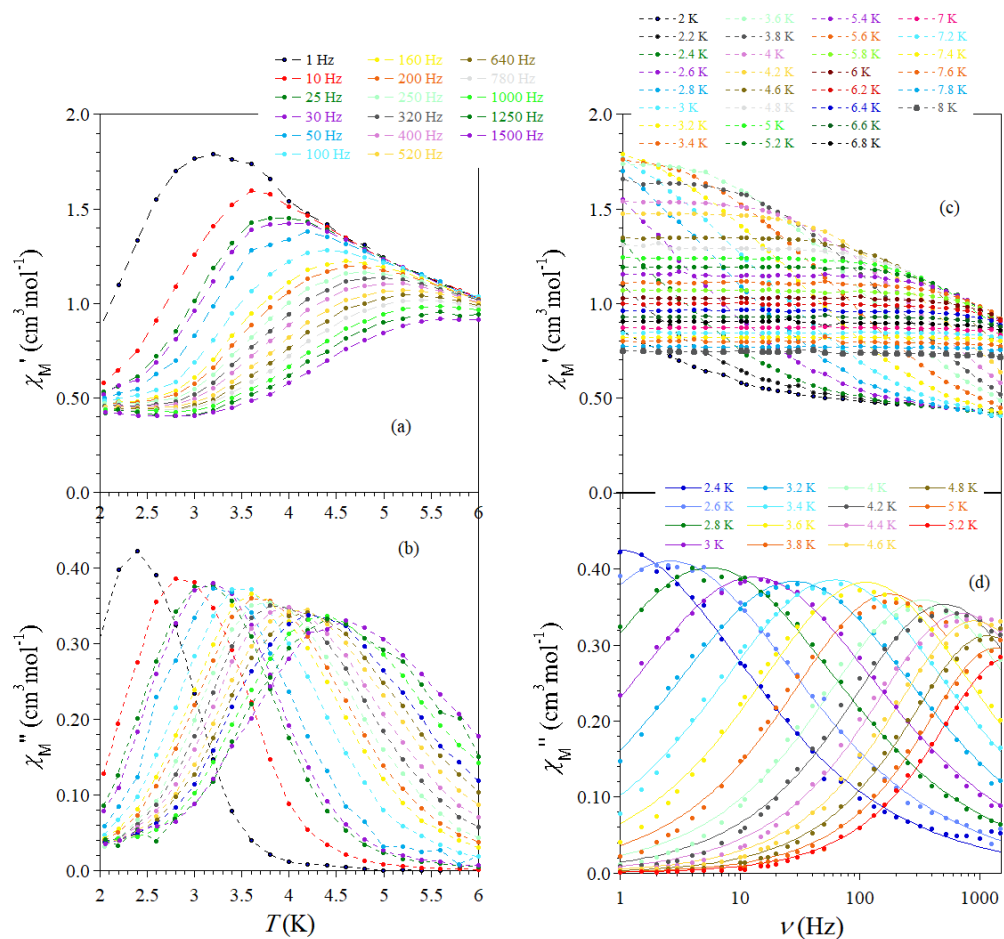
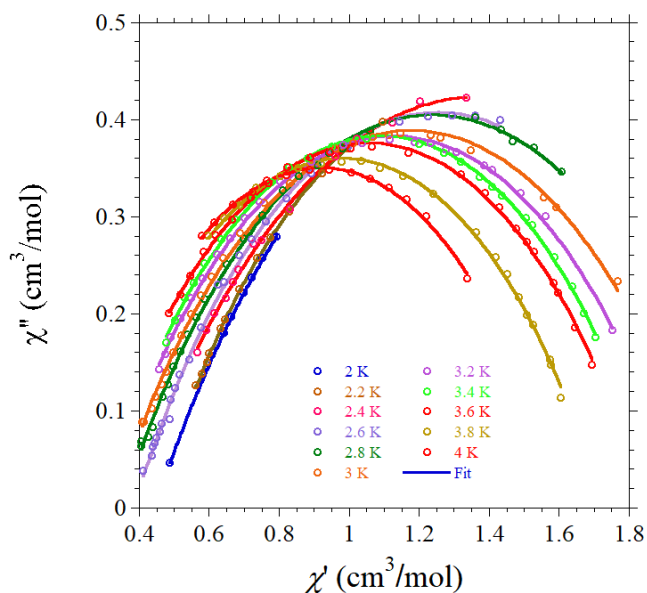


Figure SI23. Cole-Cole ($\chi_M'' = f(\chi_M')$) plots for **9** between 2 and 4 K at 1000 Oe with the best fits to the generalized Debye model (equation 1)⁴; the best fit parameters are given in the table.

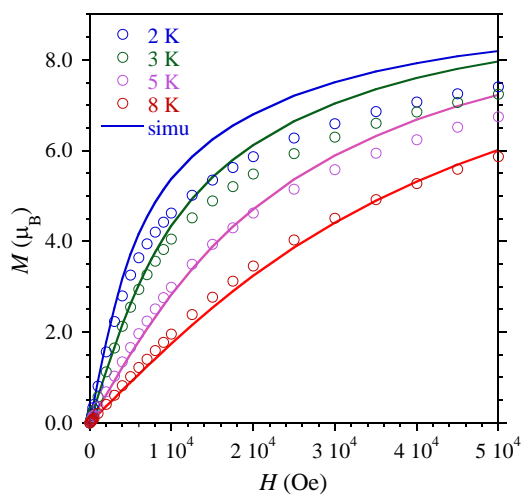


T (K)	χ_T ($\text{cm}^3 \text{mol}^{-1}$)	χ_S ($\text{cm}^3 \text{mol}^{-1}$)	α	R^2
2	2.5668	0.4426	0.47038	0.99996
2.2	2.1943	0.44392	0.43113	0.99987
2.4	2.3457	0.37714	0.48285	0.99897
2.6	2.1228	0.38302	0.4421	0.99921
2.8	2.1273	0.3474	0.45615	0.99929
3	2.0326	0.32529	0.45543	0.99898
3.2	1.9543	0.30225	0.44667	0.99916
3.4	1.8873	0.29508	0.42834	0.99931
3.6	1.8488	0.26402	0.43545	0.99877
3.8	1.7221	0.23953	0.424	0.9988
4	1.607	0.23203	0.39946	0.99753

$$\chi'' = (\chi_T - \chi_S) \tan\left(\frac{\pi\alpha}{2}\right) + \sqrt{\left[\left(\frac{\chi_T - \chi_S}{2}\right)^2 \left\{ \left[\tan\left(\frac{\pi\alpha}{2}\right) \right]^2 + 1 \right\} - \left(\chi' - \frac{\chi_S + \chi_T}{2}\right)^2\right]} \quad \text{equation 1}$$

Figure SI24. Calculated (full lines) and experimental (O) $M = f(H)$ behaviors for **8** and **9**. The calculated curves have been obtained using the full set of parameters yielded by the theoretical calculations for each complex (Table 1).

Compound 8



Compound 9

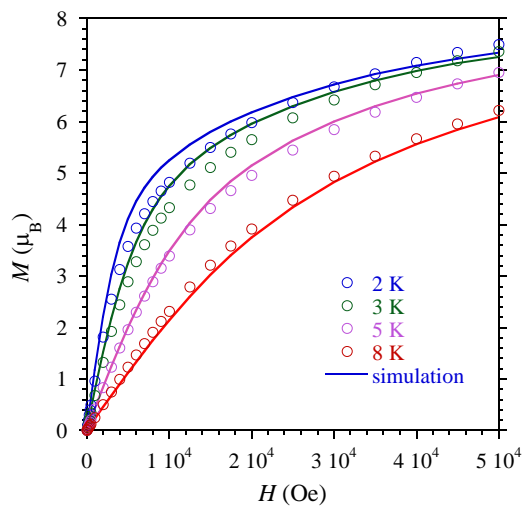


Table SI12. Coordinates of the symmetric molecular fragment used as model complex. Distorted complexes can be easily obtained from these coordinates.

Fe	0.000000	0.000000	0.000000
N	0.000000	2.300000	0.000000
N	2.086164	0.842865	0.000000
N	-2.086164	0.842865	0.000000
O	1.452323	-1.657029	0.000000
O	-1.452323	-1.657029	0.000000
N	0.000000	0.000000	-2.110000
N	0.000000	0.000000	2.110000
C	0.000000	0.000000	-3.260000
C	0.000000	0.000000	3.260000
C	2.352291	2.094894	0.000000
C	-2.352291	2.094894	0.000000
C	1.156329	2.932315	0.000000
C	-1.156329	2.932315	0.000000
C	1.188563	4.321942	0.000000
C	0.001229	5.044671	0.000000
C	-1.188563	4.321942	0.000000
N	-3.080805	-0.084653	0.000000
N	3.080805	-0.084653	0.000000
C	2.660542	-1.378090	0.000000
C	-2.660542	-1.378090	0.000000
H	-0.023026	6.133401	0.000000
H	-2.144039	4.844424	0.000000
H	-3.387991	2.431413	0.000000
H	-4.066778	0.124922	0.000000
H	-3.389225	-2.187375	0.000000
H	2.144039	4.844424	0.000000
H	3.387991	2.431413	0.000000
H	4.044760	0.210058	0.000000
H	3.389225	-2.187375	0.000000

Figure SI25. MOs (from left to right) : d_{xz} , d_{yz} , $d_{x^2-y^2}$, d_{xy} and d_{z^2} of the symmetric model complex.

